



KE200X DEGREE PROJECT IN CHEMICAL ENGINEERING,  
SECOND CYCLE, 30 CREDITS  
*STOCKHOLM, SWEDEN 2022*

# Physics-Based Modelling for SEI and Lithium Plating During Calendar and Cycling Ageing

Oskar Nordlander

## **Author**

**Oskar Nordlander**

Chemical Engineering for Energy and Environment  
KTH Royal Institute of Technology

## **Place for Project**

**Volvo Cars**

Gothenburg, Sweden

## **Examiner**

**Göran Lindbergh**

Applied Electrochemistry  
KTH Royal Institute of Technology

## **Supervisors**

**Kristian Frenander**

**Anderson Smith**

Volvo Cars

## **Date**

June 30, 2022

## Sammanfattning

Målet med projektet var att undersöka samt implementera en fysikbaserad DFN modell för att simulera kalender samt cykling åldrande av litiumbatterier som används i elbilar. Den fysikbaserade modellen var konstruerad baserad på ett Python bibliotek vid namn PyBaMM, vilket till skillnad från datadrivna modeller ger essentiell information om de kemiska processerna inuti batteriet. Den första delen av projektet täcker konceptet av kalenderåldring, vilket inkluderar en jämförelse mellan tre olika hastighetsbegränsande SEI modeller. Parametrar som påverkar det erhållna resultatet från modellen är identifierade, estimerade, och till slut validerade för att säkerhetsställa att modellen och parametrarna är identifierbara gentemot experimentella data. Resultatet av jämförelsen gav att SEI tillväxt begränsad av lithium interstitiell diffusion är den mest optimala modellen att applicera när kalenderåldring för litiumbatterier ska modelleras. Resultaten visade också att endast en parameter, inre SEI lithium interstitiell diffusivitet ska justeras för att erhålla optimal anpassning mot experimentella data. Andra delen av projektet använde resultatet från den första delen och lithium plätering implementerades som en andra åldringsmekanism som undersöktes under tre olika laddningsprotokoll. Modellen var optimerad och anpassad gentemot experimentella data, där parametervärdet för kinetisk hasighetskonstanten för plätering var estimerad. Den optimerade modellen användes därefter för att erhålla mer information om elektrokemiska variabler för att kunna analysera samt beskriva åldringsprocessen utan att behöva genomföra praktiska laborationer. Resultaten visade att mängden pläterat lithium på den negativa elektroden ökade för celler som var exponerade till högre ström under laddningsprocessen, samt när cellerna var laddade vid höga SoC nivåer. Sammanfattningsvis, visade modellen hög potential att representera och evaluera experimentella data, samt tillhandahålla en inblick i elektrokemiska processer och kapacitetsförluster länkade till SEI tillväxt och lithium plätering. Däremot, för att erhålla en högre grad noggrannhet av elektrokemiska åldringsmekanismer i lithiumbatterier, fler ytterligare mekanismer måste implementeras såsom mekanisk stress av både negativ och positiv elektrod.

---

**Nyckelord** - Litium-jonbatterier, Kalenderåldring, Cykling åldrande, Batteriåldrande, Fysikbaserad Modellering, SEI, Lithium Plätering

## Abstract

The aim of this study was to investigate and apply a physics-based DFN model to simulate the calendar and cycling ageing of lithium-ion batteries manufactured for EV applications. The physics-based cell ageing model was constructed based on the open-source software Python library PyBaMM, which in comparison to data-driven models provides more essential information about the chemical process within the battery cell. The first part of the project covers the concept of calendar ageing which includes comparisons between three different rate-limiting SEI growth models. Parameters that affect the output from the physics-based model are isolated, estimated with numerical methods, and lastly validated to ensure that the model and the parameters represent the physics behind the experimental data. It was found that the SEI growth limited by lithium interstitial diffusion is the most optimal model to apply for a physics-based model when modeling calendar ageing. It was also found that the only parameter that should be tuned against experimental data is the inner SEI lithium interstitial diffusivity. The second part of the project utilizes the results from the first part and introduces lithium plating as a second cell ageing mechanism under three different charging protocols. The model was optimized and fitted against experimental data by sweeping the lithium plating kinetic rate constant parameter. The optimized model was thereafter used to generate outputs that more thoroughly can explain the degradation effects of the cell without constructing real-world experiments. Where increased rate of plated lithium could be observed for the cell subjected to higher charging C-rate, and when the cells were charged at high SoC levels. To summarize, the model showed great potential in representing and evaluating the experimental data and providing the project with insight into the electrochemical processes and cell capacity losses of SEI growth and lithium plating. However, in order to achieve a higher accuracy of cell ageing model in relation to the lithium-ion cells used in customer vehicles, several additional cell degradation mechanisms have to be introduced, such as mechanical degradation of the two electrodes.

---

**Keywords**— Lithium-ion Battery, Calendar Ageing, Cycling Ageing, Battery Degradation, Physics-Based Modelling, SEI, Lithium Plating

# Contents

|          |   |           |
|----------|---|-----------|
| <b>1</b> | <b>Introduction</b>   | <b>1</b>  |
| 1.1      | Background to Lithium-ion Batteries . . . . .                     | 1         |
| 1.2      | Electrification of Transportation Sector . . . . .                | 3         |
| 1.3      | Previous Degradation Studies of EVs . . . . .                     | 3         |
| 1.4      | Aim . . . . .   | 4         |
| <b>2</b> | <b>Background</b>   | <b>5</b>  |
| 2.1      | Cell Ageing Mechanisms . . . . .                                  | 5         |
| 2.1.1    | Solid Electrolyte Interface . . . . .                             | 5         |
| 2.1.2    | Lithium Plating . . . . .   | 8         |
| 2.1.3    | Connecting SEI Growth & Lithium Plating . . . . .                 | 9         |
| 2.1.4    | Gas evolution . . . . .   | 10        |
| 2.1.5    | Surface Cracking . . . . .  | 11        |
| 2.2      | Defining State of Charge . . . . .                                | 11        |
| 2.3      | Modelling Cell Ageing . . . . .                                   | 12        |
| 2.3.1    | Doyle-Fuller-Newman Model . . . . .                               | 12        |
| 2.4      | Implementation of Models . . . . .                                | 14        |
| 2.4.1    | Python Battery Mathematical Modelling . . . . .                   | 14        |
| 2.4.2    | Experiments & Parameter Estimation . . . . .                      | 16        |
| 2.4.3    | Parameter & Model Validation . . . . .                            | 17        |
| <b>3</b> | <b>Methodology</b>  | <b>18</b> |
| 3.1      | Delimitations . . . . .   | 18        |
| 3.1.1    | Calendar Ageing . . . . .   | 18        |
| 3.1.2    | Cycling Ageing . . . . .  | 18        |
| 3.2      | Assumptions . . . . .   | 18        |
| 3.2.1    | Calender Ageing . . . . .   | 18        |
| 3.2.2    | Cycling Ageing . . . . .  | 19        |
| 3.3      | Modelling Calendar Ageing with SEI . . . . .                      | 19        |
| 3.3.1    | Data Visualization & Model Implementation . . . . .               | 19        |
| 3.3.2    | Identifying & Estimating Affecting Parameters . . . . .           | 20        |
| 3.3.3    | Parameter & Model Validation . . . . .                            | 20        |
| 3.4      | Modelling Cycling Ageing with SEI & Lithium Plating . . . . .     | 21        |
| <b>4</b> | <b>Results &amp; Discussion</b>                                   | <b>22</b> |
| 4.1      | Calendar Ageing with SEI Growth . . . . .                         | 22        |
| 4.2      | Arrhenius Relation & Calendar Ageing Model Optimization . . . . . | 27        |
| 4.3      | Calendar Ageing Model Comparison & Validation . . . . .           | 33        |
| 4.4      | Cycling Ageing with SEI & Lithium Plating . . . . .               | 38        |
| <b>5</b> | <b>Conclusion</b>   | <b>49</b> |
| 5.1      | Calendar Ageing . . . . .   | 49        |
| 5.2      | Cycling Ageing . . . . .  | 49        |
| <b>6</b> | <b>Future Work</b>  | <b>51</b> |

|   |           |
|---|-----------|
| <b>A Appendix</b>                                 | <b>56</b> |
| A.1 Figures . . . . .                             | 56        |
| A.2 Governing Equations for DFN Model . . . . .   | 58        |
| A.3 PyBaMM Parameters . . . . .                   | 60        |
| A.3.1 Cell . . . . .                              | 60        |
| A.3.2 Electrolyte . . . . .                       | 60        |
| A.3.3 Experiment . . . . .                        | 60        |
| A.3.4 Negative electrode . . . . .                | 61        |
| A.3.5 Positive electrode . . . . .                | 61        |
| A.3.6 Separator . . . . .                         | 62        |
| A.3.7 Lithium plating . . . . .                   | 62        |
| A.3.8 SEI . . . . .                               | 62        |
| A.3.9 Standard Values of SEI Parameters . . . . . | 63        |

## Acronyms

**BEV** Battery Electric Vehicle. 3, 57

**C-rate** Current Rate. ii, 2, 3, 5, 8, 9, 21, 39, 41, 42, 44, 46, 48, 50, 51

**DCIR** Direct Current Internal Resistance. 21, 35–38, 49

**DFN** Doyle-Fuller-Newman. i, ii, iv, 4, 12–15, 18–23, 25–33, 35, 36, 38, 48, 58

**EV** Electric Vehicle. ii, 3, 49, 51

**HEV** Hybrid Electric Vehicle. 3, 56

**LIB** Lithium-ion Battery. 1–10, 12, 14, 18, 19, 21–23, 32, 48, 49, 51, 56

**OCV** Open Circuit Voltage. 1, 11, 12, 33, 42–48, 50

**PHEV** Plug-in Hybrid Vehicle. 3, 57

**PyBaMM** Python Battery Mathematical Modelling. i, ii, 4, 14–16, 18–21, 25, 27, 29, 30, 32–35, 37, 41, 48, 49, 51, 63

**SEI** Solid Electrolyte Interface. i–iv, vi, 4–11, 18–25, 27, 29, 30, 32–39, 41, 42, 44, 46, 48–51, 63

**SoC** State of Charge. i, ii, 2, 3, 7–12, 19–38, 42, 46, 48, 49, 51

## Nomenclature

|                          |  |                 |   |
|--------------------------|--|-----------------|---|
| $\alpha_{a,Li}$          | Anodic lithium transfer coefficient    | $E_a$           | Activation energy                                 |
| $\alpha_{ox}^{v_{ox}}$   | Activity oxidized species              | $E_{cathode}$   | Cathode open circuit voltage                      |
| $\alpha_{red}^{v_{red}}$ | Activity reduced species               | $E_{cell}$      | Cell voltage                                      |
| $\beta_3$                | Cathodic lithium transfer coefficient  | $E_{OCV}$       | Cell open circuit voltage                         |
| $\delta$                 | Lithium plating thickness              | $F$             | Faraday's constant                                |
| $\Delta\phi$             | Difference in surface potential        | $I$             | Current   |
| $\eta_a$                 | Anodic overpotential                   | $j_0$           | Exchange current density                          |
| $\eta_c$                 | Cathodic overpotential                 | $j_{pl}$        | Lithium plating current density                   |
| $\eta_{li}$              | Lithium plating overpotential          | $j_{sei}$       | SEI current density                               |
| $\eta_{sei}$             | SEI overpotential                      | $j_{tot}$       | Current density porous interphase                 |
| $\frac{A}{A_0}$          | Arrhenius relation                     | $L_0$           | Initial SEI thickness                             |
| $\kappa_{eff}$           | Electrolyte conductivity               | $L_{sei}$       | SEI thickness                                     |
| $\phi_e$                 | Electrostatic potential in electrolyte | $N$             | Cycle number                                      |
| $\phi_s$                 | Electrostatic potential in electrode   | $n$             | Number of electrons transferred in redox reaction |
| $\sigma_{\pm}$           | Solid particle's conductivity          | $Q_{irr}^{sei}$ | Irreversible capacity losses to SEI               |
| $\varepsilon$            | Porosity                               | $R$             | Universal gas constant                            |
| $A$                      | Anode surface area                     | $r$             | Spherical particle radius                         |
| $A_{crack}$              | Crack surface area                     | $R_i$           | Resistance  |
| $c_{EC,0}$               | Initial solvent concentration          | $R_{li}$        | Lithium plating resistance                        |
| $c_{EC}$                 | Solvent concentration                  | $R_{sei}$       | SEI resistance                                    |
| $c_e$                    | Lithium concentration in electrolyte   | $T$             | Temperature                                       |
| $c_{Li}$                 | Plated lithium concentration           | $t$             | Time  |
| $D_{\pm}$                | Solid-phase diffusion coefficient      | $t^+$           | Cation transference number                        |
| $D_{EC}$                 | Solvent diffusion constant             | $U$             | Intercalated lithium potential                    |
| $D_{eff}$                | Electrolyte diffusion coefficient      | $V$             | Mean particle volume                              |
| $E_{anode}$              | Anode open circuit voltage             | $x_i$           | Fraction of lithium concentration                 |

# 1 Introduction

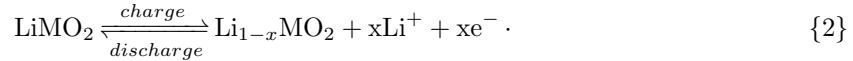
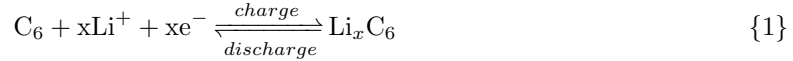
## 1.1 Background to Lithium-ion Batteries

Electrochemical energy storages have a key role in improving both stationary and mobile technologies in various sectors. There are currently vast number of different technologies available on both research and market level, where the Lithium-ion Battery (LIB) technology currently excels in terms of maturity, power- energy density, and cycle life.[1] The term LIB does not originate from the cell components but rather the charge storage mechanism between the positive and negative electrode of the battery cell. Whereas the electrochemically active and inactive materials of the cell determine the cell performance and properties. Furthermore, electrochemically active materials of the LIB are anode, cathode, and electrolyte while the inactive materials are current collector, binder and separator.[1] Anode materials utilized are predominantly made of graphite or amorphous carbon structures due to the relative reversibility of the intercalation process of  $\text{Li}^+$ .[2] A summary of available cathode compositions paired with carbon anode for LIBs depending on field of application can be seen in Table 2. A graphical comparison between the cathode compositions can be seen in Figure 28 in Appendix A.1.

Table 1: Summary of different cathode composition used in LIBs.[3]

| Material<br>Unit   | Capacity<br>$\text{Ah kg}^{-1}$ | Potential V | Energy density<br>$\text{Wh kg}^{-1}$ |
|--|---------------------------------|-------------|---------------------------------------|
| <b>NCA</b> $\text{LiNi}_x\text{Co}_y\text{Al}_{1-x-y}\text{O}_2$ | 200                             | 3.7         | 740                                   |
| <b>LCO</b> $\text{LiCoO}_2$                                      | 160                             | 3.9         | 624                                   |
| <b>NMC</b> $\text{LiNi}_x\text{Mn}_y\text{Co}_{1-x-y}\text{O}_2$ | 160                             | 3.7         | 592                                   |
| <b>LMO</b> $\text{LiMn}_2\text{O}_4$                             | 100                             | 4.1         | 410                                   |
| <b>LFP</b> $\text{LiFePO}_4$                                     | 160                             | 3.4         | 544                                   |
| <b>LFMP</b> $\text{LiFe}_{0.15}\text{Mn}_{0.85}\text{PO}_4$      | 150                             | 4.0/3.4     | 590                                   |

One common electrode configurations of a LIB cell is graphite and NMC, such as  $\text{C}_6/\text{LiMO}_2$ . The reason behind this its increase in popularity in certain sectors is the high energy density.[3, 4] The electrochemical reactions for the arbitrary graphite anode and NMC cathode are defined with respectively ( $0 \leq x \leq 1$ ) according to following reactions



The electrochemical driving force of a battery including LIBs is the potential difference between the electrodes within the cell when no current is applied and both half-cell reactions are at equilibrium, this is often referred to as the Open Circuit Voltage (OCV) and can the relation can be seen in (1).[5] Moreover, the cell potential changes when a current is applied, resulting in a decreasing or increasing of  $\text{Li}^+$  activity in the electrolyte depending on the direction of reaction seen in Reaction 1 and 2.[4] The difference in potential during non-standard activities is described by Nernst equation.[6] Which is described as the following expressions

$$E_{\text{OCV}} = OCV_{\text{cathode}} - OCV_{\text{anode}}. \quad \{1\}$$

$$E_{cell} = E_{OCV} + \frac{RT}{nF} \cdot \ln \left( \frac{\alpha_{ox}^{v_{ox}}}{\alpha_{red}^{v_{red}}} \right). \quad (2)$$

Furthermore, the potential difference between the electrodes within the cell can also be described with anodic and cathodic overpotentials, applied current and the resistance of the different parts of the cell.[7] The relation of the different contributions to the overpotential is defined as

$$E_{cell} = E_{OCV} - |\eta_a| - |\eta_c| - I \left( \sum_{i=1}^n R_i \right). \quad (3)$$

Since the potential drop over the cell and the overpotentials of the two electrodes both depend on the current, the cell potential drop as the operating current increases. The relation between the cell potential and the operating current depends on the cell configuration. Moreover, the energy losses of a battery cell increases with increasing current leading to increase in temperature which reduces the cell potential according to (2). A visualization of the relation between cell voltage and operating current can be seen in Figure 1.

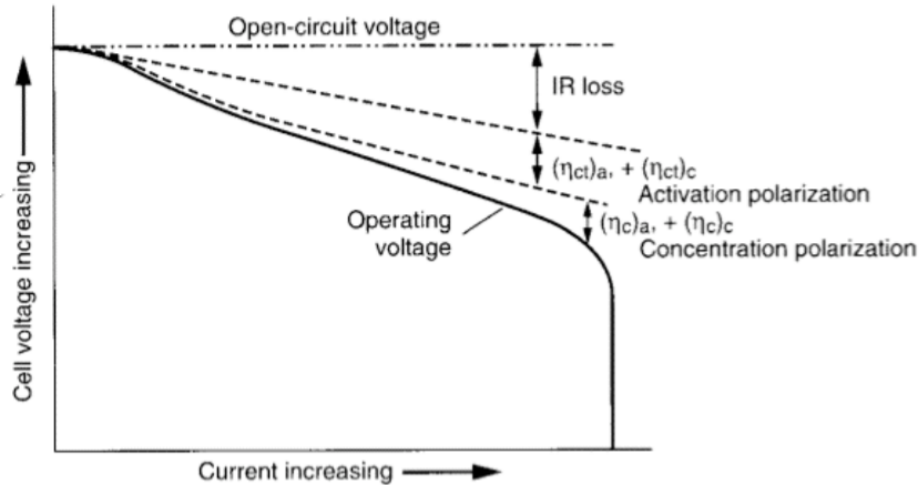


Figure 1: Cell potential as a function of operating current.[7]

The operating current during charge and discharge of a cell is often referred to as Current Rate (C-rate). Where 1 C is the current induced to charge or discharge the cell in 1 hour. A 3.6 Ah capacity LIB operating static at 1 C is discharging and charging at  $\pm 3.6$  A. If the C-rate of the battery increases to 2 C the current induced increases two-fold and the charge and discharge time is halved. In correlation to C-rate, the amount of energy stored in a battery based on its maximum capacity is often referred to as State of Charge (SoC). Where 100% SoC is fully charged and 0 % SoC is fully discharged. Moreover, batteries and especially LIB are capable to dynamically convert chemical energy into electrical energy of different rates depending on load, making it a perfect fit for mobile applications with non-static in power profiles such as electronics and vehicles.

## 1.2 Electrification of Transportation Sector

As of 2017, transportation, electricity- and heat generation sectors account for two thirds of the global green house gas emissions. Where road passenger transportation accounts for three quarters of the emissions in the transportation sector alone.[8] Therefore, outphasing the traditional internal combustion engine and accelerating vehicle electrification plays a vital role in reducing greenhouse gas emissions and mitigating climate change. Where the versatility of the LIB technology has potential to substitute and possibility to replace the internal combustion engines completely.[9]

There are three main types of Electric Vehicle (EV) available to the market with different characteristics. Hybrid Electric Vehicle (HEV) and Plug-in Hybrid Vehicle (PHEV) are two hybrid technologies which both utilize an internal combustion engine, traction battery pack and an electric motor. Where the battery in HEV can only be charged from regenerative braking , while PHEV can both be charged while driving and connected to the grid. The third type is BEV which has a larger traction battery and electric motor that solely powers all functions of the vehicle.[10, 11, 12] A visualisation of the different components in each EV technology can be seen in Figure 29-31 in Appendix A.1.

Since every drive of a vehicle is different from the other, the propulsion system needs to be able to adapt the difference in the power profiles. Therefore, EVs batteries have also to be capable to dynamically change the C-rate when needed at different levels of SoC. Additionally, consumers wants long range and fast charging EVs. These desirable characteristics of EVs are causing a trilemma in relation to cell lifetime, since they intensify a higher rate of degradation of battery cell.[13]

## 1.3 Previous Degradation Studies of EVs

One common misconception is to believe that the battery cells installed in different configurations EV technology is dominated by cell degradation only during charge and discharge. Where the cycle ageing has received a lot of attention, to prolong the lifetime but also improve essential characteristics of the battery cells, such as fast charging and longer range.[14] However, calendar ageing has gained more attention in recent years and has shown to be dominating cause to battery degradation in EVs. Calendar ageing is essential when no current flows through the battery cell which can be related to when EVs are parked, which can exceed  $> 90\%$  of the time during life of a vehicle.[15]

Furthermore, previous degradation studies have shown that the rate of cell degradation related to calendar ageing is highly dependent on the storage temperature and the SoC of the battery cells. Where the rate of cell degradation linked to calendar ageing is governed by parasitic reactions and thermodynamically instabilities, and cycle ageing is governed by kinetic effects such as concentration gradients and mechanical stress. However, recent studies have shown that the rate of degradation of LIBs can in fact be highest at the interval between 70-80 % SoC, which has been known as "spoon" profile behavior when speaking of calendar ageing.[14]

The cell ageing mechanisms that causes capacity fade from calendar and cycle ageing will be presented in Section 2.1. The importance to investigate the behaviour of the battery packs ageing with different power profiles at different temperatures for manufacturers is increasing not least in automotive industry. Furthermore, scientists and engineers are working to more accurately simulate the behaviour of battery cells to decrease time and cost of development.

## 1.4 Aim

This thesis project aims at investigating the open-source battery modelling software PyBaMMs DFN model capability of modelling calendar ageing with SEI growth and cycling ageing with connected SEI growth and lithium plating as cell ageing mechanisms. This is conducted by comparing three different rate-limiting DFN models for SEI growth to experimental data obtained from Volvo Cars and estimating parameters that affect the capacity degradation of the LIB cell. Hence, also try to describe at which conditions during calendar and cycling ageing the rate of cell degradation is highest. The optimized models will thereafter be utilized to obtain more information by simulating and visualizing results that were not gathered as experimental data but are available as model output in PyBaMM.

## 2 Background

### 2.1 Cell Ageing Mechanisms

The total capacity of LIB decreases over time as a result of mechanical and electrochemical processes, which is influenced by various operating conditions of the cell during its lifetime. In the following section some of the most dominant ageing mechanisms that degrades the capacity of LIBs will be presented.

#### 2.1.1 Solid Electrolyte Interface

Solid electrolyte interface (SEI) formation is one of the most dominating cell ageing mechanism in C<sub>6</sub> based LIBs, if not the most dominating during moderate conditions and initial stages of cycling.[16] The SEI formation and continuing growth is assumed to have an Arrhenius dependence upon the temperature, meaning that that SEI formation will occur at a faster rate at higher temperatures.[17] SEI formation is initiated from the first formation cycle, which is usually performed at lower C-rates to ensure as uniform SEI-layer as possible on the surface of the electrodes. Where the purpose of layer is to protect the electrode to further react with the electrolyte and preventing exfoliation of graphene layers on the anode.[4, 18] However, due to the porous structure of the SEI-layer species that takes part in the formation are still able to diffuse through the growing SEI-layer and react. Hence, as the SEI-layer thickens less reactive species are able to diffuse to the active surfaces, which gives SEI growth a characteristic  $\sqrt{t}$  dependency of the capacity fade of the LIB cells.[16, 19] Various reaction paths can occur depending on the local conditions. However, the most common one modelled by researchers is the reaction between intercalated Li<sup>+</sup> and ethylene carbonate which is an electrolyte solvent in most LIBs. The reaction between Li<sup>+</sup> and ethylene carbonate in presence of electrons forms lithium ethylene dicarbonate, most commonly known as SEI. Where the absence of electrons causes the reaction to occur at a slower rate, hindering the formation of extensive SEI. The reaction of the formation of SEI can be seen in Reaction 3.[20] A summary schematic of the competing intercalation process of Li<sup>+</sup> and SEI formation limited by solvent diffusion and lithium interstitial diffusion can be seen in Figure 3.

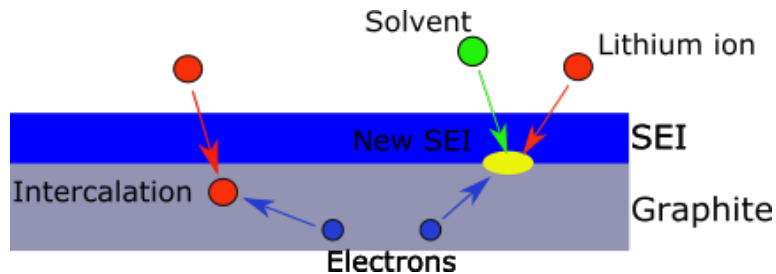
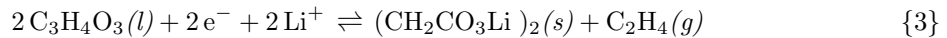


Figure 2: Schematic of competing reactions at electrode surface with solvent diffusion limited SEI growth.

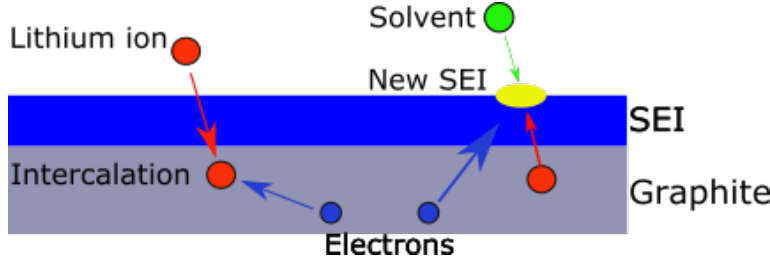


Figure 3: Schematic of competing reactions at electrode surface with lithium interstitial diffusion limited SEI growth.

Conducting experimental studies to understand the continuous growth of the SEI-layer is highly complex theoretically. In order for modelling and simulating the SEI growth effect on LIBs capacity, researchers have to assume a rate limiting step of Reaction 3. Furthermore, SEI growth and related irreversible capacity losses caused by the long term growth mechanisms and the current density of the SEI-layer  $j_{sei}$  can be expressed as (4) independently of what step of the SEI formation processes is assumed to be the rate limiting according to

$$\frac{\partial Q_{irr}^{sei}}{\partial t} = \pm A j_{sei}^i. \quad (4)$$

The thickness of the homogeneous SEI-layer as a function of the irreversible capacity losses from (4) can be expressed as

$$L_{sei} = \frac{VQ_{irr}^{sei}}{sAF} + L_0. \quad (5)$$

Where the irreversible capacity losses to SEI-growth is denoted as  $Q_{irr}^{sei}$ , V is the mean particle volume, s is the stoichiometric coefficient of Li in Reaction 3.  $L_0$  is the initial thickness of SEI-layer, A is the surface area of the anode, and F is Faraday's constant. Furthermore, the most common assumption applied according to previous modelling studies of SEI is that the rate of reaction is kinetically limited.[20]. The kinetically limited step can be expressed by a Tafel equation which can be seen in (6).[18, 20, 19] Where the exchange current density of the SEI-layer  $j_{0,sei}^{kin}$  is a fitting constant. Additionally, the overpotential caused by the kinetically limited SEI growth can be expressed as

$$j_{sei}^{kin} = -j_{0,sei}^{kin} \exp\left(\frac{-\alpha nF}{RT}\eta_{sei}\right) \quad (6)$$

$$\eta_{sei} = E_{anode} + \eta_{anode} - E_{sei} + R_{sei}LI. \quad (7)$$

Another common assumption in SEI growth modelling is assuming that the solvent diffusion is the rate limited step of reaction.[20] Under this assumption the current density of SEI can be approximated according to Fick's law of diffusion. Where the bulk concentration of solvent  $c_{EC,0}$  is set to constant,  $D_{EC}$  is the pre-defined diffusion constant,  $c_{EC}$  is the concentration in the porous structure of the electrode.[19] The expression for diffusion limited stage is defined as

$$j_{sei}^s = -FD_{EC}\nabla c_{EC} \approx -FD_{EC}\frac{c_{EC,0}}{L}. \quad (8)$$

A similar assumption model to the solvent diffusion model described in (8) which is the interstitial diffusion model of lithium. Which also can be approximated according to Fick's Law of diffusion as

can be seen in (9).[19] Where  $x = 0$  denotes the electrode and SEI interface and  $x = L$  denotes SEI and electrolyte interface according to

$$j_{sei}^{Li} = -FD_{Li}\nabla c_{Li} \approx -FD_{Li} \frac{c_{Li|x=L} - c_{Li|x=0}}{L}. \quad (9)$$

The lithium interstitial concentration difference in the SEI seen in (9) includes  $c_{Li|x=L}$  which is equal to 0 since the SEI growth is limited by diffusion and all lithium reacts when reaching the interphase, and the unknown parameter of  $c_{Li|x=0}$  and cannot be directly evaluated or estimated. Hence, in order to estimate the difference in lithium interstitial concentration, an additional assumption has to be applied. Where the electrochemical potential of the intercalated lithium in the negative electrode is set to be equal to the lithium in the SEI.[19] Which is defined as

$$U_{C_6}^{Li} = U_{SEI}^{Li} = U_{SEI,0}^{Li} RT \ln \left( \frac{c_{Li|x=0}}{c_{Li,max}} \right). \quad (10)$$

Where  $U_{SEI,0}^{Li}$  denotes a constant reference value,  $c_{Li,max}$  is the maximum concentration of intercalated lithium at 100 % SoC. The electrochemical potential of intercalated lithium ions in the negative electrode  $U_{C_6}^{Li}$  is equal to  $-FU$ . By applying the lithium interstitial concentration at 0 V denoted as  $c_{Li,0}$  which includes all constant contributions from (10).[19] A final expression for estimating  $c_{Li|x=0}$  can be derived according to

$$c_{Li|x=0} = c_{Li,0} \exp \left( \frac{-FU}{RT} \right) \quad (11)$$

The different rate limiting mechanisms have different inputs that affect the overall capacity loss and current density, which can be seen from (4) and (9). Hence, the rate limiting assumptions depend on that different species have diffuse through a certain layer or have certain reaction kinetics and overpotentials. Moreover, in the interstitial-diffusion limited assumption the Li atoms must deintercalate and diffuse through the SEI-layer and react at the SEI – electrolyte interface. While solvent-diffusion assumes that the solvent must diffuse through the SEI-layer and form SEI at the electrode surface. The reaction limited assumption is not limited by the diffusion of any species, but rather the kinetics of the reaction and formation of SEI itself. Therefore, for the interstitial-diffusion limited assumption, the concentration of lithium atoms at the interphase between the SEI and the electrolyte is assumed to be zero, and that lithium reacts as it reaches the interphase. The solvent-diffusion limited assumes a concentration profile where the concentration of the electrolyte solvent at the electrode and SEI interphase is zero, and that the solvent reacts as it reaches the interphase. Moreover, the reaction-limited model is not limited by the diffusivity of a reactive species, hence the species does not automatically react leading to an arbitrary concentration of the species at the surface limited by the kinetics of the reaction.

It has been shown through experiments that the capacity degradation caused by SEI growth in LIBs has a  $\sqrt{t}$  dependence. This dependency results in a rapid degradation in the beginning of cell ageing and eventually declines over later stages of the ageing process. Hence, the different rate limiting models for simulating the growth of SEI should also follow the same pattern of dependency in order to achieve a correct fit to experimentally observed data of SEI growth. All of the rate limiting SEI models shown in (6) - (9) besides the reaction kinetic model are able capture such behaviour. In reaction limited model the SEI resistivity is typically resulting in a weak dependency on the thickness of the SEI-layer which promotes a linear dependence during cell ageing.

In addition to the time dependence of the rate limiting models the capacity fade of SEI growth is also SoC dependent. This implies that the rate limiting models should include a term for the potential

difference in SEI in order to account for different levels of SoC. All rate limiting models are able to capture the SoC dependency except for the solvent diffusion limited model, which does not account for potential difference over the SEI layer but rather only the bulk concentration of the solvent. Therefore, the solvent diffusion model is able to capture the  $\sqrt{t}$  dependency of the SEI growth, while not being able to capture SoC dependence of SEI growth.[17]

### 2.1.2 Lithium Plating

After extended amount cycling of LIBs, the capacity degradation transition to more nonlinear behavior. Which indicates that an additional cell ageing mechanism is taking place within the cell. Previous cell ageing studies have reported thick  $\text{Li}^+$  layer deposition near the  $\text{C}_6$  anode and separator regardless of the cathode composition. However, lithium plating usually occurs at high rate during low operating temperatures, high SoC levels, and at high C-rates during charging of LIBs.[21] The reasoning for its occurrences at later stages of the cell life is due to equilibrium potential of lithium intercalation being only 100 mV higher than the equilibrium potential of lithium deposition reaction during charging.[22] Hence, as the cell is ageing and SEI-layer thickens the electrode pores is less accessible resulting in reduced anode ionic kinetics and the competitiveness between the two reactions increases.[23, 20] The expressions for irreversible lithium plating is similar to kinetic limited SEI in (6) and (7) and is described as

$$j_{pl} = j_{0,pl} \exp \left( \frac{\alpha n F}{RT} \eta_{li} \right) \quad (12)$$

$$\eta_{li} = E_{anode} + \eta_{anode} - E_{li} + R_{li} \delta I. \quad (13)$$

Where  $E_{anode}$  and  $\eta_{anode}$  denotes the negative electrode potential and overpotential,  $E_{li}$  and  $R_{li}$  denotes the equilibrium potential and the resistance of the plated lithium respectively.[20] It has previously been shown that lithium plating can be reversible, resulting in mitigation of the lost capacity and nonlinear ageing behavior.[24] The reversible reaction of lithium plating is often referred to as lithium stripping. Furthermore, during the discharging process the plated lithium can be dissolved as  $\text{Li}^+$  and can be utilised further in later cycles. However, if the  $\text{Li}^+$  are fully covered by extensive growth of SEI, lithium plating results to irreversible capacity losses of the cell. This phenomenon is often referred to as dead lithium in literature and previous scientific studies.[25]

Furthermore, lithium plating has often been identified as only occurring while  $\eta_{li}$  in (13) and (14) reaches negative values. However, scientists have been able to show that this is not the case and it occurs at all values of  $\eta_{li}$ , but rather that the rate of lithium plating is rapidly increased with negative values of  $\eta_{li}$ . Moreover, the rate of lithium plating mechanisms is as previously described heavily influenced by the temperature, SoC levels, and C-rates especially during the charging process. To fully understand the root cause behind these statements, one can break down the charging processes into three major steps:[26]

1.  $\text{Li}^+$  diffuses out from the cathode.
2.  $\text{Li}^+$  are diffusing while being dissolved in the electrolyte.
3.  $\text{Li}^+$  ions diffuses through the SEI layer and intercalates within the anode.

While the cell operates during lower temperatures the transport of  $\text{Li}^+$  occurs at a slower rate, this is due to the reduced diffusivity and charge transfer kinetics of the intercalation process of  $\text{Li}^+$  in lower

temperatures. This leads to a bottleneck effect with high local  $\text{Li}^+$  concentrations at the electrode interphase which stimulates the lithium plating reaction. Increasing the C-rate during the charging process will increase the transport rate of  $\text{Li}^+$  while being rate limited by the diffusion of  $\text{Li}^+$  through the SEI and. This also leads to a bottleneck effect with high local  $\text{Li}^+$  concentrations at the electrode interphase which stimulates the lithium plating reaction. Similar to the two previous cases, during high SoC levels fewer active sites in the anode are available to stimulate the intercalation process for  $\text{Li}^+$ , which also results in high local  $\text{Li}^+$  concentrations at the electrode interphase which stimulates the lithium plating reaction.[26, 27] A cross section schematic of the three charging conditions where lithium plating is significantly increased can be seen in Figure 4.

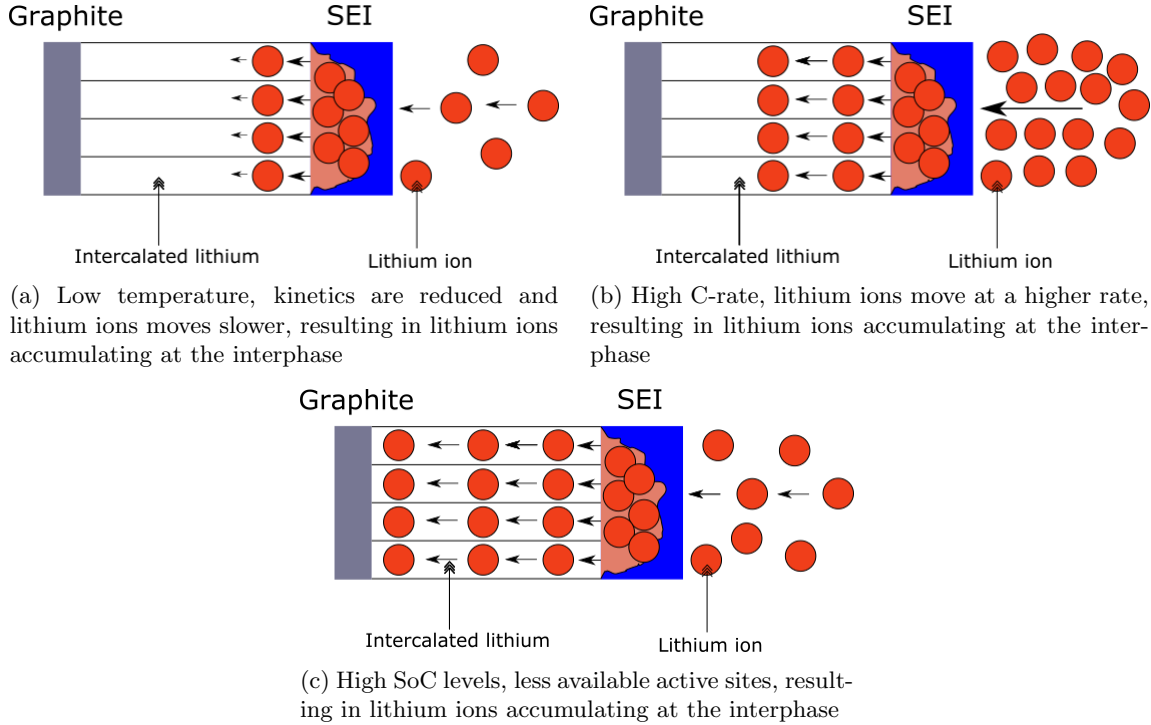


Figure 4: Cross-section schematic of the negative electrode and SEI, under those charging conditions where lithium plating formation is significantly increased. Deposition of lithium occurs at the interphase where the local concentration of lithium ions is high due to the different operating conditions during charging.

### 2.1.3 Connecting SEI Growth & Lithium Plating

Since SEI growth and lithium plating described in Section 2.1.1 and 2.1.2 both are parasitic reactions in LIB, it is important to define how they affect one and another. Previous modeling studies whose goal has been to present and describe the correlation between the SEI growth and lithium plating, have defined the lithium plating potential as a function of the SEI overpotential which is defined in (7). The correlation between the SEI and lithium plating is defined as

$$\eta_{li} = \Delta\phi - \eta_{sei}. \quad (14)$$

The term  $\Delta\phi$  ( $\phi_s - \phi_l$ ) in (14) represent the difference in surface potential of the negative electrode. Moreover,  $\Delta\phi$  will vary under cycling of a LIB cell. Reaching its highest value at 0 % SoC and its lowest and possible negative value at 100 % SoC where the maximum concentration of intercalated lithium in the negative electrode is reached. Furthermore, a standard Butler-Volmer expression for the reaction flux is derived as (15). However, to obtain an accurate correlation between the overpotentials of SEI growth and lithium plating and capacity losses connected to each degradation mechanism, a Butler-Volmer expression for the flux can be derived. Which utilizes set transfer coefficients of  $\alpha_{a,Li}$  and  $\alpha_{c,Li}$ , and includes the correlation shown in (14) for SEI and lithium plating.[27] The correlating Butler-Volmer expressions are defined as

$$N_{Li} = k_{Li} \left( c_{Li} \exp \left( \frac{F\Delta\phi}{2RT} \right) - c_e \exp \left( -\frac{F\Delta\phi}{2RT} \right) \right) \quad (15)$$

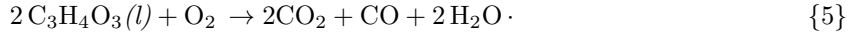
$$N_{Li} = k_{Li} \left( c_{Li} \exp \left( \frac{F\alpha_{a,Li}\eta_{Li}}{RT} \right) - c_e \exp \left( -\frac{F\alpha_{c,Li}\eta_{Li}}{RT} \right) \right). \quad (16)$$

#### 2.1.4 Gas evolution

Among the most energy dense cathode compositions for LIBs which can be seen in Table 1, the majority tries to maximise the nickel content in order to increase the specific capacity of the electrode. NMC cathode compositions have been connected to that cyclability of the cell coincides with gas evolution at the cathode surface. Hence, the gas evolution in the LIBs with high nickel content are connected to cell ageing and capacity degradation through a “shuttle” reaction of  $\text{CO}_2$  generation.[28] This reaction instead damages the cell performance by irreversibly depleting the  $\text{Li}^+$  within the cell by forming lithium oxalate according to following reaction



Previous scientific studies have concluded that the reaction path of lithium oxalate formation originates from the formation of singlet oxygen evolution at the active surface of the cathode. Where scientist have assumed that the gas evolution is an electrochemical reaction which depends on the local electrode. However, recent studies have shown that it is a pure chemical reaction of the material composition of the electrode which depends on the SoC and not the voltage. Furthermore, it has also been proven through on-line electrochemical mass spectrometry that the singlet oxygen evolution from the NMC cathode is highest at the crucial threshold at 80 % SoC.[29] Additionally, from the singlet oxygen evolution at the active surface of the cathode, the singlet oxygen can further react with the electrolyte solvent ethylene carbonate resulting in  $\text{CO}_2$  and  $\text{CO}$  evolution.[30]. According to following reaction



Estimations have shown that oxidation of ethylene carbonate which can be seen in Reaction 5 occurs at higher potentials, and results in a slow potential drop of NMC electrode during storage and self discharge. Furthermore, the scientific community is gathering more evidence that the singlet oxygen evolution is linked to  $\text{CO}_2$  evolution within LIBs after several analytical studies. Which in theory poses a severe challenge for future developments of chemically stable NMC electrodes since it is not a pure electrochemical reaction path but rather a chemical reaction.[29, 30]

$\text{CO}_2$  can potentially be titled one of the most significant consumptions reactions in LIBs, often referred to as the “shuttle” reaction which can be seen in Reaction 4. Where two  $\text{CO}_2$  forms the intermediate of the soluble oxalate  $\text{C}_2\text{O}_4^{2-}$  after receiving two electrons from the anode, which compared to SEI

formation can diffuse to the cathode which makes it a reversible reaction. Hence, this also can finalize the “shuttle” loop where the oxalate effectively transports two electrons and is accompanied by two  $\text{Li}^+$  and forming irreversible lithium oxalate.[14, 30]

### 2.1.5 Surface Cracking

Surface cracking is caused by expansions and contractions of the electrodes as  $\text{Li}^+$  intercalates and extracts. Furthermore, battery cycling leads to mechanical stress in the electrodes, which propagate crack formation and fatigue of the material.[20] As crack formation occurs, new surface area gets exposed to electrolyte promoting new SEI-layer formation, which results in less  $\text{Li}^+$  that can be utilized during future cycles. Therefore, previous scientific studies have concluded that mechanical stress of the electrodes must be taken in considering when constructing a mathematical model of battery degradation. Where the expression of surface cracking is based on Paris' law for crack growth, the derived expression for surface cracking is described as

$$\frac{\partial A_{\text{crack}}}{\partial N} = \beta_3 (x_{\max} - x_{\min})^2. \quad (17)$$

Where  $A_{\text{crack}}$  denotes the increase of crack surface area,  $N$  is the cycle number with fitting parameter  $\beta_3$  and  $x_i$  denotes fraction of lithium concentration.[20, 31]

## 2.2 Defining State of Charge

In order to be able to characterise cell ageing mechanisms outlined in Section 2.1 with highest possible accuracy, the SoC needs to be defined for the specific cell interesting for investigation. An approach suggested by previous scientific studies is to define the stoichiometric coefficient “x” for OCV curves for the anode and cathode half-cell. Moreover, the stoichiometric coefficients for the different capacity levels of the cell can be estimated by fitting empirical equations denoted  $U_a$  and  $U_c$  for each respective electrode to experimental data.[32] Hence, the OCV curve of the full cell and its SoC dependence can be determined by balancing the expression of the electrode is defined as

$$OCV(SOC) = U_c ((x_{c,100\%} - x_{c,0\%}) SOC + x_{c,0\%}) - U_a ((x_{a,100\%} - x_{a,0\%}) SOC + x_{a,0\%}). \quad (18)$$

In (18)  $x_{0\%}$  and  $x_{100\%}$  denote each half-cells stoichiometric coefficients at 0 and 100 % SoC respectively.  $U$  denotes the expression for the experimental fit as a function of the stoichiometric coefficients for each half-cell at specific capacity levels of interest. By applying the expression shown in (18) one can translate the SoC levels to capacity or vice-versa correctly according to the specific cell chemistry and electrode composition.[32] The OCV curve utilized in this project can be seen in Figure 5.

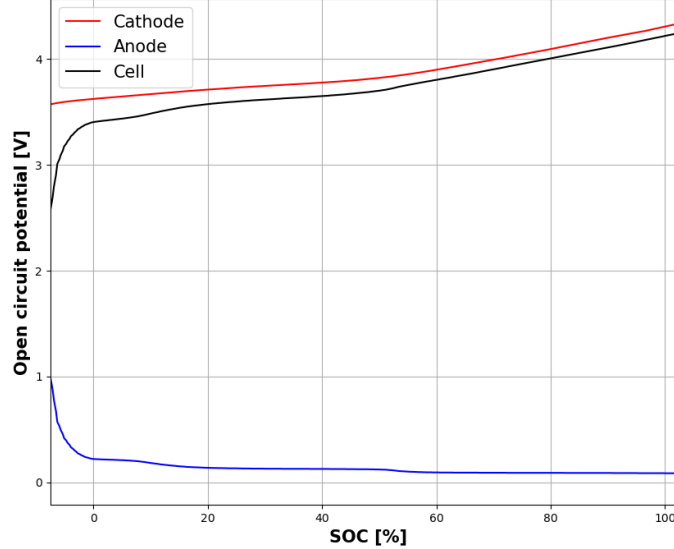


Figure 5: OCV as a function of SoC for half-cells and full cell used in the project.

## 2.3 Modelling Cell Ageing

In order to describe the cell behavior of LIBs in accordance with the ageing mechanisms outlined in Section 2.1 different type of models categories needs be implemented. Where the most accurate models in complete cell behavior are the electrochemical engineered models.[20] In the following sections two of the most popular electrochemical engineered model for LIB ageing will be presented individually.

### 2.3.1 Doyle-Fuller-Newman Model

The Doyle-Fuller-Newman (DFN) model also referred to as the pseudo-two-dimensional model, is a model built upon porous electrode theory and solving systems of highly-coupled nonlinear partial differential equations.[33] The model assumes that at every point of the electrode there is a spherical particle that represent the active material of the cell, where there is a spatial dimension for the electrode thickness and another dimension for the radius of the individual active particles. An illustration of this can be seen in Figure 6.[33, 34]

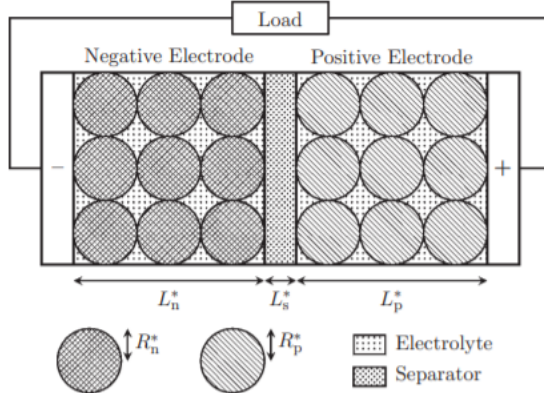


Figure 6: Illustration of spatial dimensions of DFN model.[33]

Moreover, DFN is the most standardised model simulating  $\text{Li}^+$  transport and diffusion in two dimensions of a cell.[20]. The governing equations of the DFN model are based on the charge and molar conversion and electrochemical reactions. The system of partial differential equations are solved by various different numerical methods, the DFN can be seen as unnecessary for coupled-system applications due to the computational power and time needed to solve the model. However, the model is undoubtedly one if not the most powerful method for estimating, optimising and predicting battery cell performance. Geometric, kinetic and thermodynamic properties are input parameters, that results in over 30 different output parameters which describes and characterises the chemical, electrochemical and physical properties of the cell.[34] The governing equations of the DFN model describe and solves four scalar fields from four different differential equations which can be seen in (19) – (22). Where the differential equations describe the electrostatic potential  $\phi_e(x, t)$  and  $\phi_s(x, t)$  in the electrolyte and solid electrode respectively. Followed by the concentration of  $\text{Li}^+$   $c_e(x, t)$  and  $c_a(x, r, t)$  in the electrolyte and the active material of the electrode. The governing equations, initial, and boundary conditions of the system of asymptotic derived partial differential equations for the DFN model can be seen in Appendix A.2, a full explanation to the equations and the asymptotic derivation can be found in the referenced resource.[33]

$$j_{tot} = \sigma_{\pm} \frac{\partial^2 \phi_s}{\partial x^2} \quad (19)$$

In (19) the charge conversion of the electrode is given by Ohm's law, where  $j_{tot}$  denotes the current across the porous interphase between electrode and electrolyte.  $\sigma_{\pm}$  denotes the solid particle's conductivity in either negative or positive electrode.[35] For the electrostatic potential of the electrolyte an additional non ohmic term is being added, which can be described by the expression

$$j_{tot} = -\kappa_{eff}(c_e, T) \frac{\partial^2 \phi_e}{\partial x^2} + \frac{2RT}{F} \kappa_{eff}(c_e, T) (1 - t^+) \frac{\partial^2 \ln c_e}{\partial x^2}. \quad (20)$$

$t^+$  denotes the cation transference number, and  $\kappa_{eff}(c_e, T)$  denotes the conductivity of the electrolyte. The continuity equation for  $\text{Li}^+$  in the electrolyte is defined by a diffusion and source term, as according to

$$\frac{\partial(\varepsilon c_e)}{\partial t} = \frac{\partial}{\partial x} \left( \frac{\partial c_e}{\partial x} D_{eff}(c_e, T) \right) + j_{tot} \left( \frac{(1 - t^+)}{F} \right). \quad (21)$$

$\varepsilon$  denotes the porosity, and  $D_{\text{eff}}(c_e, T)$  denotes the electrolyte diffusion coefficient at different electrolyte concentrations and temperatures. Lastly, the  $\text{Li}^+$  concentration in the particles of the electrode accounts for the diffusion in radial dimension  $r$  of spherical particles and the diffusion coefficient  $D_{\pm}(c_a, T)$ .[35] The expression for  $\text{Li}^+$  concentration in the electrode is defined as

$$\frac{\partial c_a}{\partial t} = \frac{1}{r^2} \frac{\partial}{\partial r} \left( D_{\pm}(c_a, T) r^2 \frac{\partial c_a}{\partial r} \right). \quad (22)$$

## 2.4 Implementation of Models

As the electrification process of industries intensifies, the request for R&D in both stationary and mobile LIB applications increases. Where the processes of extensive battery cycling is not only time consuming but also expensive on a larger scale. Therefore, it has been essential for modelling research to develop simulation software to further promote collaboration between different fields of science.[36] COMSOL Multiphysics is the most predominant software for battery analysis and modelling simulation due to its user-friendly graphical unit interface. However, the software is closed source with high license cost. Therefore, several open source software and coding libraries for battery modelling have received attention from research community in recent years. Where the goal is to advance in the modelling research in correlation with the demand from the electrification of several market sectors.[36]

### 2.4.1 Python Battery Mathematical Modelling

Python Battery Mathematical Modelling (PyBaMM) is an open source and versatile battery modelling library created by researchers connected through Faradays Institution. Where the goal of PyBaMM is to achieve reliable, fast and flexible modelling software for electrochemical energy storages.[37] PyBaMM achieve this by utilizing differential algebraic equation, advanced differation and state of the art numerical solvers, making it is possible to solve the DFN model outlined in Section 2.3.1 in less then one tenths of a second.[38] Contributors of PyBaMM have over period of time added different cell ageing mechanisms to the simulation model based on state of the art research articles. The user can initiate flexible electrochemical experiments through "plug and play physics" according to a specific cell geometry, mesh and characteristics. An overview of PyBaMM pipeline approach for battery modelling can be seen in Figure 7. PyBaMMs architecture is based on an expression tree that encodes mathematical equations and modular components, making it possible for the user to fully customise the simulation at any stage.[36]

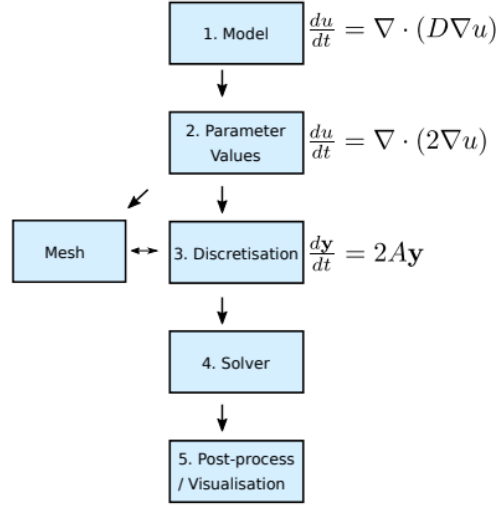


Figure 7: PyBaMMs pipeline approach of encoding user inputs and generate results.[39]

From the pipeline approach that PyBaMM utilizes which is shown from Figure 7 the user can modify each segment for individual scientific studies. The library comes pre-installed with scientific data and results, which can be optimized or adjusted for the purposes of the users intention of applying PyBaMM. Down below follows a short description of the different segments of PyBaMM pipeline approach shown in Figure 7.

### 1. Models

The user chooses what electrochemical model they want to implement for battery modelling. Available options are half-cell and full battery models. Where the DFN described in 2.3.1 is predefined, a expression tree is generated. A full transcript of the governing equations that PyBaMM utilizes for the DFN model can be seen in Appendix A.2.[39] Submodels are not mandatory to implement to the model but it complements the main models in generating a simulation that is more accurate to realistic scenarios. Hence, submodels include physics and chemistries as the degradation mechanisms described in Section 2.1. A full list of available submodels can be seen in the referenced resource.[40]

### 2. Parameter Values

Are the backbone of the model implementation in PyBaMM. Parameter values can be gathered from experimental data, physical or chemical measurements, and previous scientific litterateur covering the topic of battery parameterization. Parameters can be fixed values or functions, PyBaMM comes pre-installed with parameter sets which can be accessed in the referenced resource.[33, 34]

### 3. Discretisation

When the geometry of the model and the mesh has been set the model can be discretized with user defined spatial methods. Where variables are processed into state vectors and spatial operators into matrices.[39]

### 4. Solver

Solving the model with defined time interval. PyBaMM comes with pre-installed with numer-

ous popular ordinary differential and differential algebraic equation solvers such as Scipy and SUNIDALS.[39]

## 5. Visualization

Post processing the results from solving the model. PyBaMM has accessible visualization tools, where the data also can be exported for further analysis such as experimental data comparison.

Furthermore, the user can fully customize each stages between 1-5 in PyBaMM pipeline approach to represent a specific battery cell of investigation as accurate as possible. Which can be achieved by choosing between different models, ageing mechanisms and parameter values shown in Appendix A.3.

### 2.4.2 Experiments & Parameter Estimation

Addition to the pipeline approach introduced in Section 2.4.1, PyBaMM also has the capability to handle inputs to simulate specific experiments, or recreate experimental data by importing a drive cycle. The models can therefore be simulated identical to a physical experiment in the lab, which provides repeatability of the experiments and subsequently increases the justification and transparency to the gathered experimental results.

In order to achieve an accurate result of mathematical modelling of a battery, a calibration and parameter estimation is necessary. Which in theory is comparing the constructed model against experimental data and adjusting the model until a good fit has been achieved. This can be done by several different methods and applications, depending on the end goal of the model and simulations. Furthermore, different experimental protocols can retrieve specific parameter information. Hence, experiments such as pulse testing with rapid variating current output provide information about the kinetic parameters of the cell, while galvanostatic intermittent titration technique provide information about the thermodynamics and diffusion coefficients.[41] The parameter values within PyBaMM are divided into different sections representing each component of a cell or different ageing mechanism, this is referred to as parameter sets. The parameter sets enable the user to easy access to change the physics and chemistry of a model. A summary of all parameters that can be adjusted or evaluated within PyBaMM are listed in Appendix A.3.[36]

Evaluating and estimating key affecting parameters are fundamental for accurate battery modelling. Usually, this can be done by initially comparing model output with experimental data, while sweeping the parameters and evaluated if the model output changes. Thereafter, the parameters that do affect the model output are estimated with various numerical methods until a good fit against experimental data is achieved. A common example of this is to minimize the difference gap between the output and data according to the least square method.[42] The expression for the least square method is defined as

$$\varphi(x) = \sum_{i=0}^{i=N} (f_i(x) - d_i)^2. \quad (23)$$

Where  $x$  represent the parameter that the user wants to estimate or optimize,  $f$  is the model output variable and  $d$  is the experimental data. Several different libraries have been developed to solve local optimization problems within the Python language, where some have been tuned to tackle and solve several parameter estimations simultaneously with higher efficiently. One popular local optimization software for least square numerical method is the derivative-free optimization for least-square, which

is inspired by the Gauss-Newton with high tolerance to data noise and as the name suggest in absence of otherwise relevant derivative information.[43]

#### **2.4.3 Parameter & Model Validation**

When constructing a mathematical description of a system which are dependent on a large number of parameters, it is important to validate those parameters in order to justify the gathered modelling results. If a model and/or parameter with a set of sufficiently describes a dataset and generates a unique result, then the it's considered to be identifiable. However, if it can generate the same results with a finite amount of different sets then the model and/or parameter is considered to be non-identifiable. Non-identifiable models are essentially models that do not capture the reality of the data, and simultaneously generate a sufficiently good description of the data. Identifiability of a model is often decided after performing a statistical analysis and analysing if the mathematical expressions that describes the model in relation to data is sufficiently implemented.[44]

## 3 Methodology

In the following sections the methodology and the methods used with correlated delimitations and assumptions will be presented. The methods are presented in chronological order of the implementation phase, where the methods have been based on previous studies and theory outlined in Section 2.

### 3.1 Delimitations

- The simulation modelling will only be performed in PyBaMM, which is available for free at [www.pybamm.org](http://www.pybamm.org).
- The simulation modelling will be based on experimental data from a non-disclosed supplier of NMC811/C<sub>6</sub> LIBs
- Capacity fade caused by cell ageing mechanisms described in Section 2.1 will only be regarded and analysed.
- Experimental protocol including parameters from physical measurements were provided by Volvo Cars for simulations.

#### 3.1.1 Calendar Ageing

- Models used for simulation in PyBaMM will only be variations of different rate limiting SEI growths for the pseudo two-dimensional DFN model.
- Three rate limiting step assumptions will be implemented into three different model configurations of SEI growth.
  1. Interstitial-diffusion limited SEI model.
  2. Solvent-diffusion limited SEI model.
  3. Reaction limited SEI model.
- Parameters that are located under SEI sub-set will be analysed with each rate limiting DFN model. All the SEI parameters can be found in Appendix A.3.8.

#### 3.1.2 Cycling Ageing

- The results from the calendar ageing will be used to characterize the SEI growth during cycling ageing.
- Three experimental protocols will be analysed for the lithium plating model implementation shown in Table 2 under isothermal conditions at 25°C.

### 3.2 Assumptions

#### 3.2.1 Calender Ageing

- The DFN models are assumed to operate under isothermal conditions. Hence, there are no changes in cell temperature during calendar ageing simulations.
- The simulations will be based on capacity losses of the LIB cells, where the 100% of the lost capacity is due to SEI formation

- Only SEI-layer growth will be considered as an ageing mechanisms for the simulations.
- Inner and outer SEI-layer assume to share the same initial thickness and porosity throughout the modelling.
- For the interstitial-diffusion limited SEI model 100% of the SEI formation occurs at the SEI - electrolyte interface.
- For the solvent-diffusion limited SEI model 100% of the SEI formation occurs at the surface SEI - electrode interface.

### 3.2.2 Cycling Ageing

- The experimental protocol shown in Table 2, only considers lithium plating and SEI growth as cell ageing mechanisms during cycling.
- The kinetic rate constant for lithium plating is the only parameter that will be analysed for experimental protocol outlined in Section 3.4

## 3.3 Modelling Calendar Ageing with SEI

In the following sections the methodology for the modelling implementation of cell degradation and SEI growth will be presented. The methodology is divided into three sections, where the first section is model implementation and data visualization, second section is identifying & estimating affecting parameters, and the third section is parameter and model validation. A flowchart of each methodology section which correlated objectives in successive order can be viewed in Figure 8.

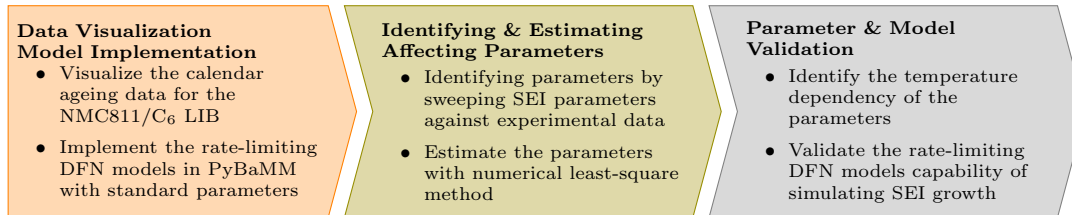


Figure 8: Process overview of modelling the capacity degradation of the NMC811/C<sub>6</sub> LIB cell.

### 3.3.1 Data Visualization & Model Implementation

The assessment of modelling and simulating calendar ageing and SEI-layer growth was conducted in several different segments. Initial stage of the modelling calendar ageing of LIB cells were analyzing and visualizing the experimental data, where the data was from calendar ageing experiment obtained from Volvo Cars. The data included calendar ageing experiments conducted at three different ambient temperatures of 25, 35, and 45 °C and at 40, 70, and 96% SoC over approximately 25,000 hours. Additionally, known parameters from physical measurements and observations of the LIB cell from the manufacturer and Volvo Cars laboratory was added to the relevant parameters within PyBaMM. The definition of the SoC levels outlined in Section 2.2 for the NMC811/C<sub>6</sub> cell were obtained prior to the simulations and parameter estimations. In order to reproduce the results in this project, the data that are being used for the modelling of calendar ageing is the average value between two data sets that have been obtained from two different cells stored under the same conditions.

Thereafter, three different DFN models were implemented in PyBaMM and compared to the experimental data. The three DFN models were constructed with different rate limiting steps of solvent diffusion limited, reaction limited, and interstitial diffusion limited SEI-growth. Description of the different rate limiting steps of SEI-growth can be found in Section 2.1.

### 3.3.2 Identifying & Estimating Affecting Parameters

A parameter sweep was conducted of all the SEI specific parameters within PyBaMM source code which can be seen in Appendix A.3.8. All the parameters that were subject to the numerical sweep process originated from literature or guesses available when installing PyBaMM and were not provided by Volvo Cars nor the cell supplier. Parameters that affected the model output in terms of capacity degradation when swept were isolated for each rate limiting DFN model. The parameters that affected the capacity degradation during the parameter sweep was estimated through numerical methods and Python libraries such as Scipy least-square and DFO-LS .[43]

After the three different DFN models had been optimized in relation to experimental data obtained from Volvo Cars, and SEI affecting parameters in PyBaMM have been estimated. The rate of cell degradation was estimated by constructing an Arrhenius plot, where the activation energies can be obtained from the value of the linear slope. The Arrhenius relation and the linearization of the relation utilized to obtain the activation energies are defined as

$$\frac{A}{A_0} = \exp\left(\frac{-E_a}{RT}\right) \quad (24)$$

$$\log\left(\frac{A}{A_0}\right) = \frac{-E_a}{R} \cdot \frac{1}{T}. \quad (25)$$

Where  $A$  and  $A_0$  represent a relation between the modelled and reference value, an example of this is the capacity fade of the cell.  $R$  is the universal gas constant,  $T$  is the temperature, and  $E_a$  is the activation energy.  $E_a$  is the minimum amount of energy needed for a chemical reaction to occur, in this case formation of excessive SEI growth outlined in Reaction 3. Hence, the affecting parameters and their estimations were analyzed from the of temperature, SoC, time, and the rate of degradation dependence. In order to achieve a holistic results for the calendar ageing process, the activation energies were calculated and evaluated at four different timestamps for each DFN model, and compared to experimental data results. The Arrhenius relation shown in (24) and the linearization in (25) will also be utilized to derive a correct temperature dependency of the diffusion parameters for the interstitial and solvent-diffusion models. Where the  $A$  and  $A_0$  relation will describe the relation between the standard value and the optimized value of the parameter.

### 3.3.3 Parameter & Model Validation

The last steps of the flowchart process shown in Figure 8 is the parameter and model validation process. This step of the model optimization process involves a comparison between the three rate limiting SEI models and a validation process study. Where dependencies such as SoC levels, SEI-layer thickness and time dependencies will be analysed in relation to the capacity fade of the cell. This study is conducted to isolate if any of the three rate limiting models are non-identifiable and should be rejected. Furthermore, also analyse and discuss if PyBaMMs SEI and DFN model have limitations in their implementation, by comparing the results with relevant research articles covering the topic of SEI growth at different SoC levels.

When the model had been fully optimized and the identity of the optimized models has been validated, the models were used to generate outputs that were not available from the experimental data of calendar ageing. These types of outputs provide additional information on the SEI-layer and were combined with the experimental data to achieve a deeper understanding of the SEI growth and cell ageing behavior. The SEI resistivity was analyzed in this project will the help of the versatile model outputs in PyBaMM. Moreover, experiments in form of Direct Current Internal Resistance (DCIR) were available as raw data from the battery supplier throughout the ageing process, where the cell had been exposed to a 10 second charge pulse followed by a 10 second discharge pulse of 3 C-rate. The difference in current and potential in-between these short pulses show the interaction effect between the internal resistance of the cell and SEI thickness, temperature, and time.

### 3.4 Modelling Cycling Ageing with SEI & Lithium Plating

When the models for SEI have been fully optimized and validated an irreversible lithium plating model will be added to the already existing cell degradation model. Where the relation between the two competing parasitic reactions of SEI growth and lithium plating will be studied and evaluated. This is conducted with three different experimental protocols which will be compared against experimental data from battery cell supplier, the different segments of each protocol can be seen in Table 2. Furthermore, the kinetic rate constant of Li-plating will be variated in order to identify a rough estimate of its value and magnitude compared to the standard value in PyBaMM.

Table 2: Experimental protocol for the cycling of LIB in PyBaMM.

| Segments                            | Protocol 1 | Protocol 2 | Protocol 3 |
|-------------------------------------|------------|------------|------------|
| SoC interval                        | 100-0%     | 100-0%     | 100-0%     |
| Cation transference number [45, 46] | 0.37       | 0.37       | 0.37       |
| Discharge until 3.38 V              | 0.33 C     | 0.33 C     | 0.33 C     |
| Rest                                | 1 hour     | 1 hour     | 1 hour     |
| Charge until 4.19 V                 | 0.33 C     | 0.66 C     | 1.00 C     |
| Hold until                          | C/50       | C/50       | C/50       |
| Cycles                              | 1200       | 1200       | 1200       |
| Temperature                         | 25 °C      | 25 °C      | 25 °C      |

The three experimental protocols that can be observed in Table 2, will as previously mentioned be implemented with the optimized SEI growth model with relevant affecting parameters. Furthermore, the longer cycling experiments are conducted in order to achieve a deeper understanding in lithium plating contribution to the ageing process, at different stages of the life in correlation to the competing reaction of SEI formation. Moreover, due to the computational expense of simulating DFN model over 1200 cycles and with two parasitic degradation reactions, only a rough estimate of the affecting parameters will be evaluated and utilized to characterize the effect of lithium plating. Where the result from the versatile PyBaMM outputs will be utilize to further describe the physics of the degradation mechanisms occurring within the cell.

## 4 Results & Discussion

In the following sections the results from the background and methodology outlined in Section 2 and 3 will be presented. Each segment of the implementation process of the methodology will be presented individually.

### 4.1 Calendar Ageing with SEI Growth

The data from the calendar ageing experiments were obtained from Volvo Cars is normalised due to confidentiality. The relative capacity fade as a function of the time at three different SoC levels and temperature utilised to optimise the DFN degradation model can be seen in Figure 9. Where the data has been converted from capacity into capacity fade as a function of time in order to observe the  $\sqrt{t}$  dependency.

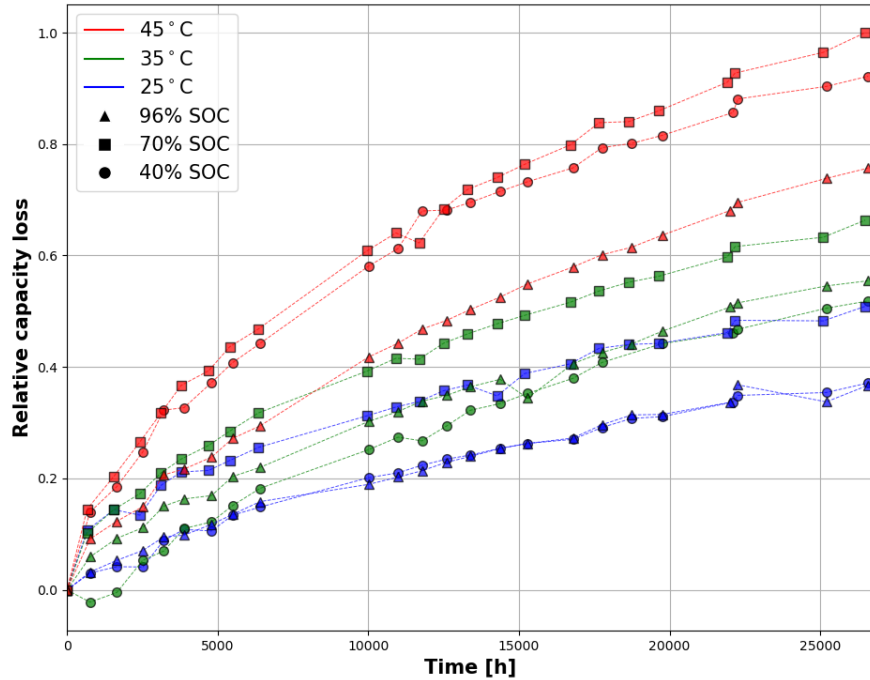


Figure 9: Relative Capacity loss between 0 and 1 as a function of time from calendar ageing experiment at three temperatures and SoC levels.

From Figure 9 it can be observed that the NMC811/C<sub>6</sub> LIB cell experiences a  $\sqrt{t}$  capacity fade dependence for all temperatures and SoC levels. Moreover, the degradation process is occurring at a higher rate in the initial stages of ageing as described in Section 2.1. This indicates that the most predominant cell ageing mechanism within the LIB cell during storage is undoubtedly SEI growth. The SEI growth and the degradation of the cell is heavily influenced by the ambient temperature during storage, which is strengthened by SEI chemical formation reaction Arrhenius dependency. However, the SoC dependency of the capacity fade experience a unique behaviour. Storage at 70% SoC results

in the highest capacity degradation of the cell at all temperatures. This behaviour could be originating from the previously described parasitic “shuttle” reaction for NMC electrodes in Section 2.1.4, where the formation of lithium oxalate increases the irreversible capacity losses even further. Surprisingly, degradation at 45°C occurs at a higher rate at 40% compared to 96% SoC, which is an indication that the spoon profile for capacity degradation SoC dependence is more influenced for lower than higher SoC levels with increased temperatures.

To be able to accurately model the experimental data of the capacity fade over time in Figure 9 the parameters affecting the SEI growth for the LIB cell needs to be estimated for each rate limiting SEI model. This allows possibilities to optimise the model which can be used to gather other important output which is not available as data from the supplier. All of the SEI parameters were swept between a 50 – 150% interval of the standard value listed in Table 12 in Appendix A.3.9. An example of the outputs from the parameter sweeps in relation to the experimental data for the three rate limiting DFN models can be seen in Figure 10.

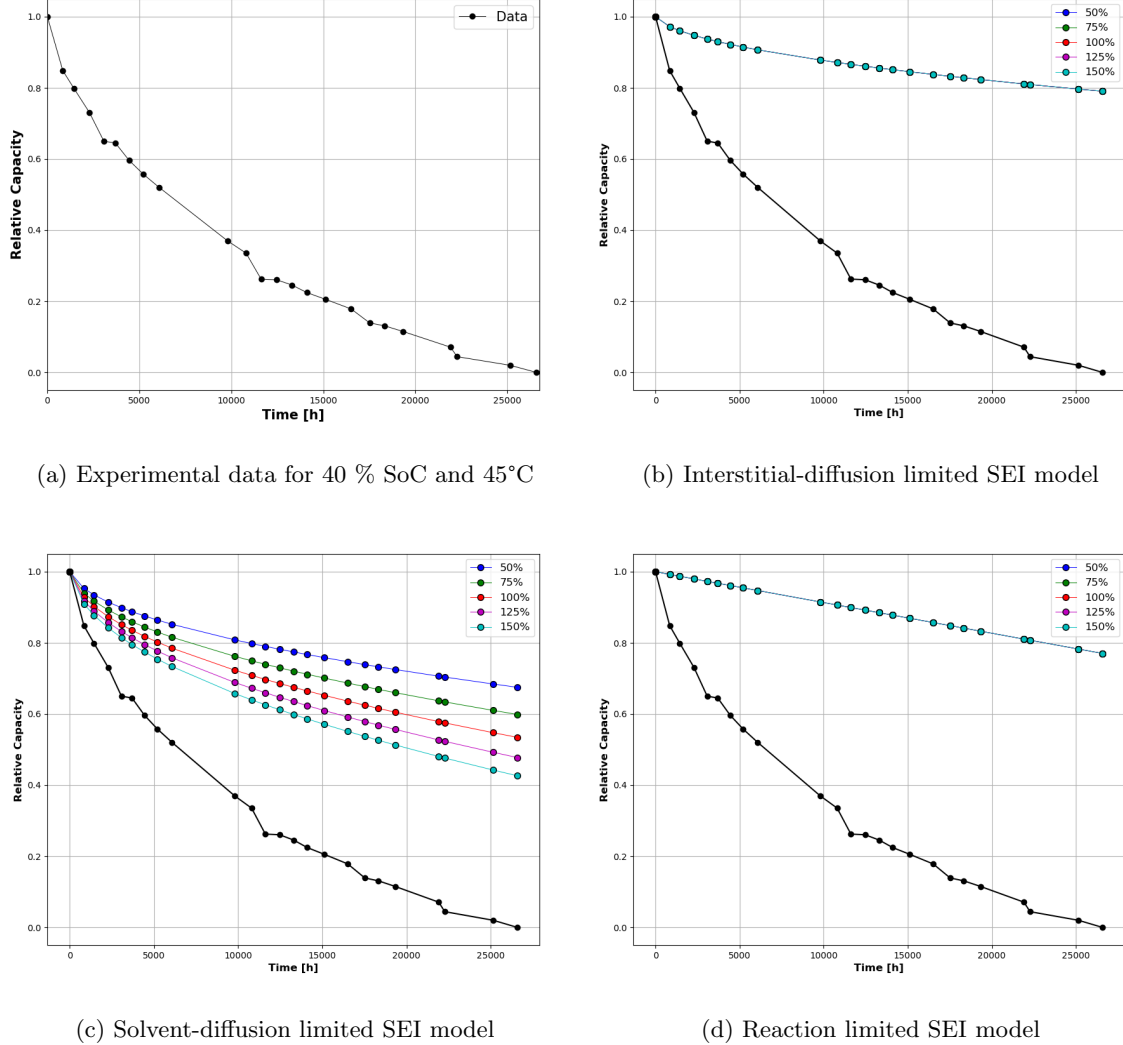


Figure 10: Relative capacity between 0 and 1 as a function of time for selected calendar ageing experiment, compared to parameter sweep of outer SEI solvent diffusivity [ $\text{m}^2 \cdot \text{s}^{-1}$ ]

The results from the parameter sweep is visualised in Figure 10 shows that the output from the solvent-diffusion limited DFN model in Figure 10c is the only rate limiting DFN model affected by the parameter sweep of the outer SEI solvent diffusivity . Meanwhile, the interstitial-diffusion model and reaction limited model is not affected by the variation of the individual parameter. This is a reoccurring phenomenon for all the parameters available in the SEI sub-set, that only one of the models is affected by increase or decrease of capacity fade. A compilation of all the affecting parameters for each rate limiting DFN model can be seen in Table 3.

Table 3: Parameters that affect the capacity degradation in each respective DFN model.

| DFN model                             | Affecting Parameters                         |
|---------------------------------------|--|
| <b>Interstitial-diffusion limited</b> | Inner SEI partial molar volume               |
|                                       | Inner SEI lithium interstitial diffusivity   |
|                                       | Lithium interstitial reference concentration |
|                                       | Initial inner SEI thickness                  |
| <b>Solvent-diffusion limited</b>      | Outer SEI solvent diffusivity                |
|                                       | Outer SEI partial molar volume               |
|                                       | Bulk solvent concentration                   |
|                                       | Initial outer SEI thickness                  |
| <b>Reaction limited</b>               | SEI kinetic rate constant                    |
|                                       | SEI reaction exchange current density        |

From Table 3 it can be seen that each individual rate limiting model have different parameters that affect the capacity degradation, either by increase or decrease the rate of degradation. Hence, the different parameters that did affect the capacity in these model simulations in PyBaMM can be identified as inputs in rate limiting equations, but also the overall capacity loss which can be seen in (4) - (9) in Section 2. The two rate limiting diffusion models shown in Table 3 are affected by the parameters that denotes the interface where the species of lithium atoms and ethylene carbonate diffuses from, but also the reference and bulk concentration respectively.

All of the affecting parameters listed for each rate limiting DFN model in Table 3 were optimised and fitted against the experimental data shown in Figure 9. This was conducted for all the different temperatures and SoC levels, resulting different values for the affecting parameters in each rate limiting model. Furthermore, the model output and the related parameters were optimised against experimental data with numerical methods outlined in Section 2.4.2, which resulted that each model only have one or two affecting parameter that should be adjusted in order to achieve the most optimised fit. The affecting parameters for each rate limiting model in Table 3 can therefore be narrowed down according to the parameters listed in Table 4. The optimised fit for each rate limiting model at the different SoC levels and temperatures can be seen in Figure 11.

Table 4: Parameters that affect the capacity degradation and achieves the most optimal fit against experimental data shown in Figure 9.

| DFN model                      | Affecting Parameters   |
|--------------------------------|--|
| Interstitial-diffusion limited | Inner SEI lithium interstitial diffusivity                         |
| Solvent-diffusion limited      | Outer SEI solvent diffusivity                                      |
| Reaction limited               | SEI kinetic rate constant<br>SEI reaction exchange current density |

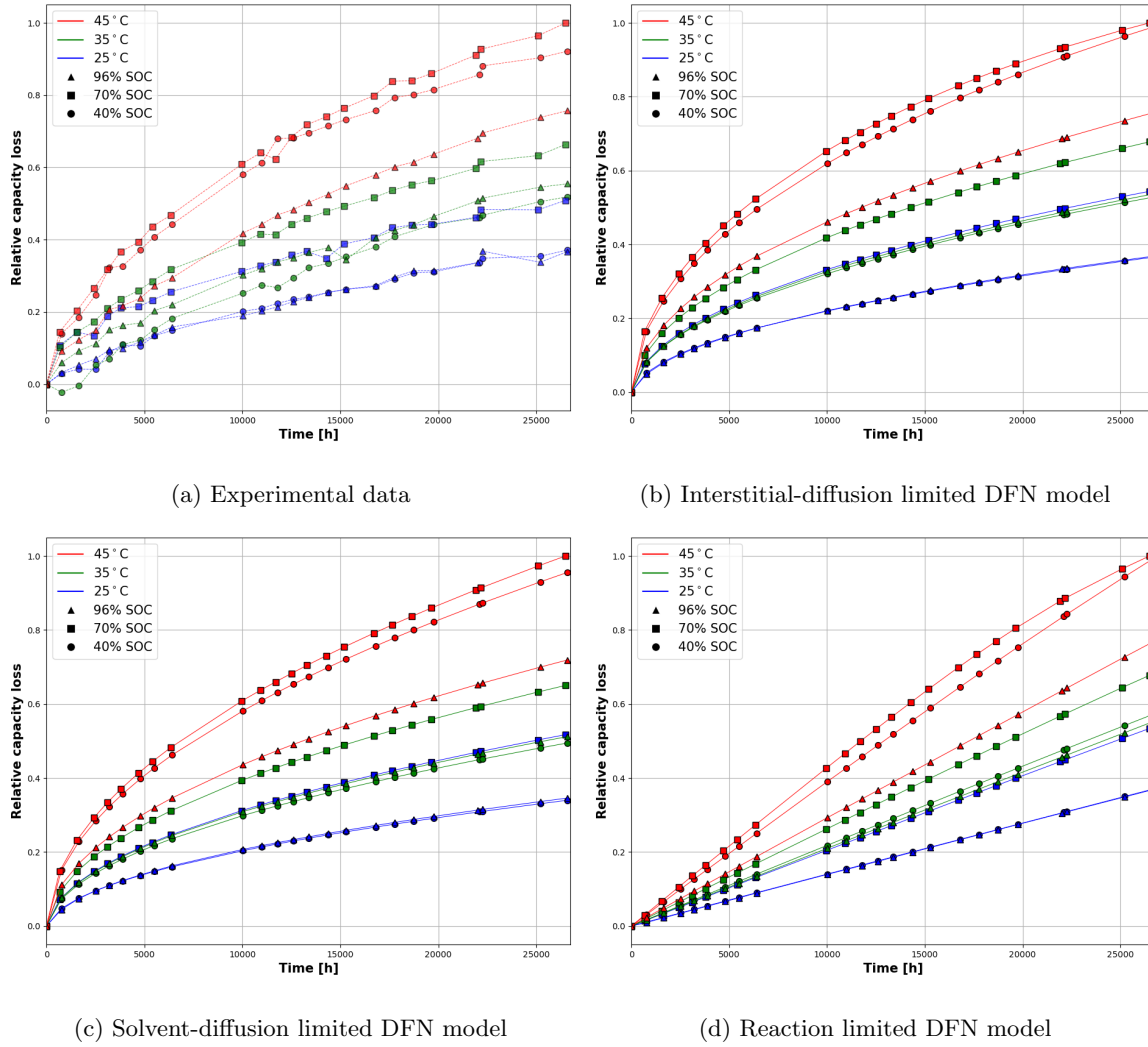


Figure 11: Relative capacity loss between 0 and 1 as a function of time for the experimental data and the three rate-limiting DFN models with temperature and SoC dependent parameters

From Figure 11d it can be observed that the reaction limited DFN model follows a linear behavior which confirms the theory described in Section 2.1.1. Since the reaction limited model cannot capture the  $\sqrt{t}$  dependence of SEI growth shown in Figure 11. Therefore, it is not a relevant rate limiting scenario to model and optimize for SEI growth caused by calendar ageing. The two diffusion-rate limiting DFN models shown in Figure 11b - 11c are able to capture the  $\sqrt{t}$  dependency of the capacity fade with relative high accuracy. The results from the optimization process of the affecting parameters shown in Table 4 yielded nine different values for each temperature and SoC levels, in reality this is not the case. This is because the two-diffusion parameters should depend on the differences in temperature and not depend on the electrode SoC. A summary of the relative parameter values shown in Table 4 and visualized in Figure 11 can be seen in Table 5.

Table 5: Relative parameter values between 0 and 1 at different temperatures and SoC levels for the two optimized rate-limiting diffusion DFN models visualized in Figure 11b - 11c.

| <b>Inner SEI lithium interstitial diffusivity</b> | <b>25°C</b> | <b>35°C</b> | <b>45°C</b> |
|---|-------------|-------------|-------------|
| 40% SoC   | 0.00        | 0.147       | 0.899       |
| 70% SoC   | 0.174       | 0.350       | 1.00        |
| 96% SoC   | 0.005       | 0.167       | 0.454       |
| <b>Outer SEI solvent diffusivity</b>              | <b>25°C</b> | <b>35°C</b> | <b>45°C</b> |
| 40% SoC   | 0.00        | 0.142       | 0.876       |
| 70% SoC   | 0.161       | 0.328       | 1.00        |
| 96% SoC   | 0.004       | 0.155       | 0.436       |

From Table 5 it can be observed that the relevant parameter value for the diffusivity parameters for both DFN model achieves the highest values at 70% SoC. Furthermore, parameter values for the diffusivity at 40% and 70% increase rapidly between 35 and 45°C for both models, which in retrospect is caused by the increase in degradation rate in the experimental as can be seen in Figure 9. However, as previously mentioned the diffusivity of lithium interstitials and solvent should experience a temperature dependence, meanwhile it should not display an electrode SoC dependence. Hence, the eighteen optimized diffusion parameters shown in Table 5 and visualized in Figure 11b - 11c have to be reduced to six parameters, three parameter values for each model one for each temperature. To find the most suitable average values of parameter values across the board with a connected SoC dependence, an Arrhenius plot can be constructed according to the relation shown in (24). Which will be followed up at the later stages of Section 4.2.

## 4.2 Arrhenius Relation & Calendar Ageing Model Optimization

From the results outlined in 4.1, the two diffusion models displaying a  $\sqrt{t}$  dependence of the capacity fade can be further analyzed by constructing an Arrhenius plot. Where the first interesting relation to analyze according to (24) is the capacity fade as a function of the temperature. The relation between the relative capacity fade output and the temperature from the two rate-limiting diffusion DFN models in PyBaMM can be seen in Figure 12.

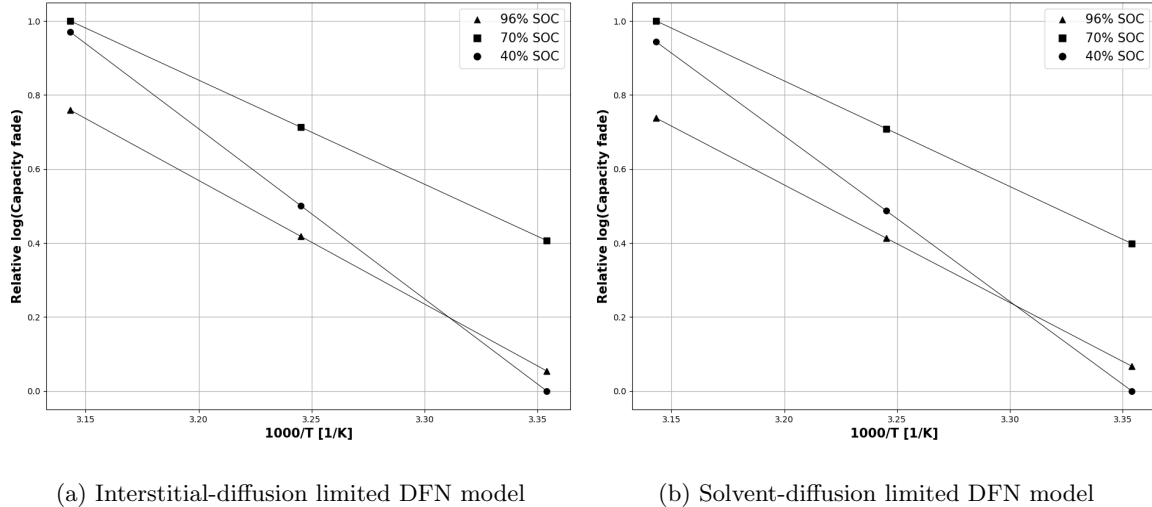


Figure 12: Relative Arrhenius relation between 0 and 1 for the capacity fade output interpolation from the rate-limiting diffusion DFN model as a function of the inverse temperature after  $\sim 2.5$  years of storage

Arrhenius relations, as previously described in Section 3.3.2 can be utilized to estimate the activation energies for certain conditions of investigation. The activation energies for the different temperatures and at each level of SoC gathered from the slope of the linear correlation as can be seen in Figure 12. An observed phenomenon is that the activation energies gathered is declining over time for 40% and 96% SoC levels, while being almost constant for 70% SoC throughout the storing period. All the relative activation energies at different stages of calendar ageing process can be viewed in Table 6. The values of the activation energies obtained from the Arrhenius relation can be correlated to the different chemical ageing processes. Similar activation energy indicates that similar chemical processes are taking place within the electrochemical cell in the same order magnitude. . However, this is evidently not the case for the different SoC levels visualized in Figure 12, which indicates that different ageing processes are more dominate at different SoC levels and temperatures.

Table 6: Relative activation energies [ $\text{kJ} \cdot \text{mol}^{-1}$ ] between 0 and 1 at different temperatures and SoC levels for the two optimized rate-limiting diffusion DFN models visualized in Figure 11b-11c

| Interstitial-diffusion limited | 3888 h | 10008 h | 14376 h | 19752 h |
|--------------------------------|--------|---------|---------|---------|
| 40% SoC                        | 1.00   | 0.917   | 0.822   | 0.857   |
| 70% SoC                        | 0.076  | 0.018   | 0.008   | 0       |
| 96% SoC                        | 0.235  | 0.162   | 0.141   | 0.120   |
| Solvent-diffusion limited      | 3888 h | 10008 h | 14376 h | 19752 h |
| 40% SoC                        | 1.00   | 0.940   | 0.923   | 0.911   |
| 70% SoC                        | 0.045  | 0.014   | 0.006   | 0.00    |
| 96% SoC                        | 0.251  | 0.203   | 0.192   | 0.181   |

The statement that different chemical ageing process is predominant at different SoC levels and temperatures is strengthen when connecting the results from the experimental data shown in Figure

9 and the values for the activation energies in Table 6. The activation energy is highest for the 40% SoC which ideally would indicate the slowest rate of degradation and least amount of SEI growth. However, this is not the case for 40% SoC and 45°C where the rate of degradation is substantially much higher compared to 96% SoC which has a lower activation energy. This might be an indication that the previously described “spoon profile” and related shuttle reaction is more influenced for lower SoC levels with increased temperature. In order to further investigate the influence of the shuttle reaction described in Section 2.1.4, the amount of parameters for each rate-limiting diffusion model have to be reduced to only have a temperature dependence. In similar manner as for the Arrhenius relations visualized in Figure 12, an Arrhenius relation between the standard parameter values and the optimized parameter values was conducted as can be seen in Figure 13.

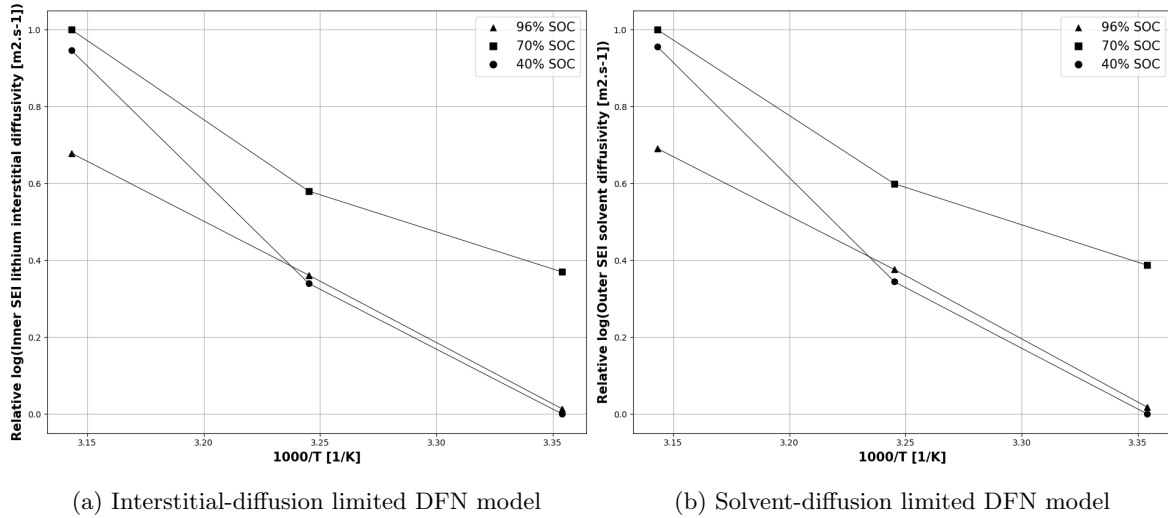


Figure 13: Relative Arrhenius relation between 0 and 1 of the standardized parameter value shown in Table 12 in Appendix A.3.9 and the optimized parameter value for each rate-limiting diffusion DFN model.

From the Arrhenius relation shown in Figure 13 it can be seen that it follows a similar linear relation for 40% and 96% SoC at lower temperatures, while 70% SoC still being an outlier. However, the temperature interval between 35 to 45°C suggest a rapid increase in value of the diffusivity parameters for 40% and 70% SoC. Moreover, Figure 13 might suggest that the model in PyBaMM adjusts for the sudden increase of degradation rate for 40% and 70% SoC which cannot be linked to SEI growth, but rather the parameter values that has been numerically optimized to fit experimental data with a temperature and SoC dependency. Therefore, three parameter values with temperature dependence for each model were derived based on extrapolation of the linear Arrhenius relation between 25°C and 35°C for all SoC levels, where SEI growth is the dominant degradation mechanism. Hence, the three parameters for each rate-limiting diffusion model were retrieved from the mean values of the extrapolated Arrhenius relation as can be seen in Figure 14.

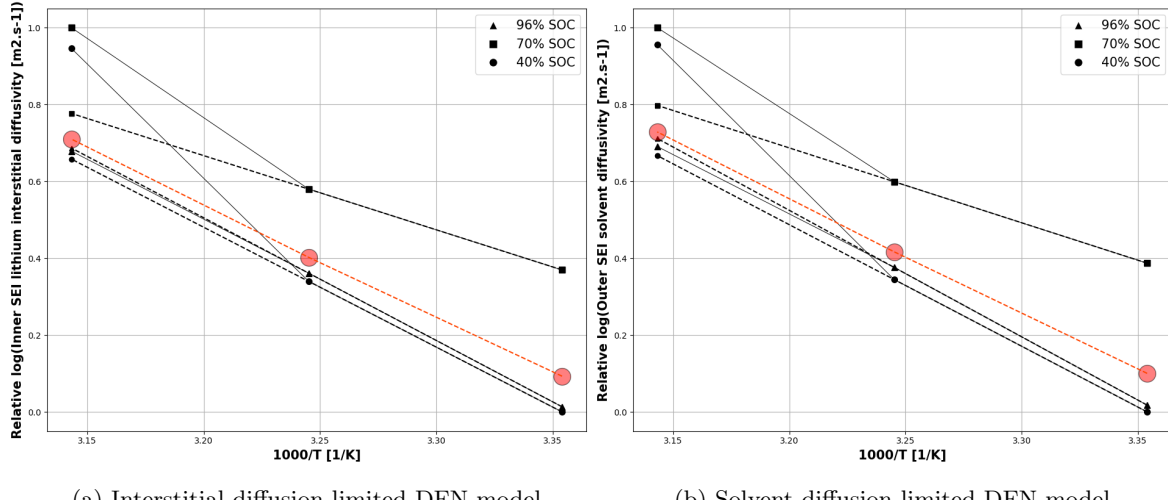


Figure 14: Relative extrapolated Arrhenius relation between 0 and 1 shown in Figure 13, which was utilized to reduce the amount of parameter values and to visualize the temperature dependence of the diffusivity

Since more than one cell ageing mechanisms are taking place within the cell, the diffusivity parameters that represent the most optimized data fit and SEI growth must be estimated at those data points where the SEI is the most dominate mechanisms. Therefore, the three parameters for the diffusivity was retrieved from the extrapolated values at lower temperatures, before the sudden increase in parameter values which can be seen in Figure 13 and 14. The newly retrieved diffusivity parameters with only a temperature dependency from Figure 14 can be seen in Table 7 and was re-introduced into the rate-limiting diffusion models. Which physically describes the capacity fade for calendar ageing if SEI growth was the only cell degradation mechanism. A comparison between the experimental data for all temperatures and SoC levels and the model output in PyBaMM temperature dependent diffusivity can be seen in Figure 15 and 16.

Table 7: Relative parameter values between 0 and 1 at different temperatures levels optimized for only considering SEI growth as a cell degradation mechanism during calendar ageing

| Inner SEI lithium interstitial diffusivity | 25°C  | 35°C  | 45°C  |
|--|-------|-------|-------|
| All SoC levels                             | 0.029 | 0.182 | 0.476 |
| Outer SEI solvent diffusivity              | 25°C  | 35°C  | 45°C  |
| All SoC levels                             | 0.033 | 0.194 | 0.504 |

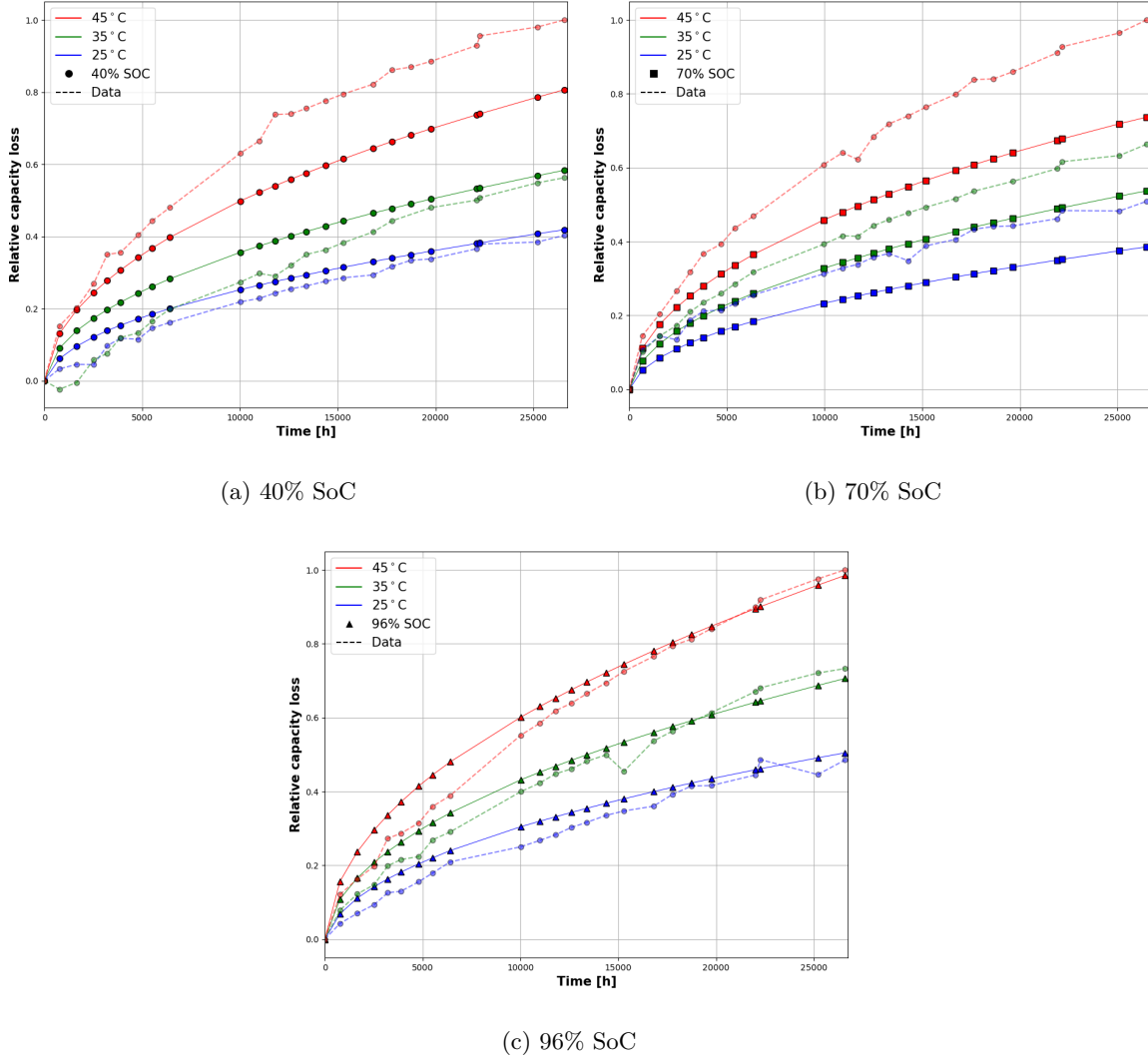


Figure 15: Relative interstitial-diffusion limited DFN model between 0 and 1 with optimized lithium interstitial diffusivity parameter with only a temperature dependency shown in Figure 14a and Table 7.

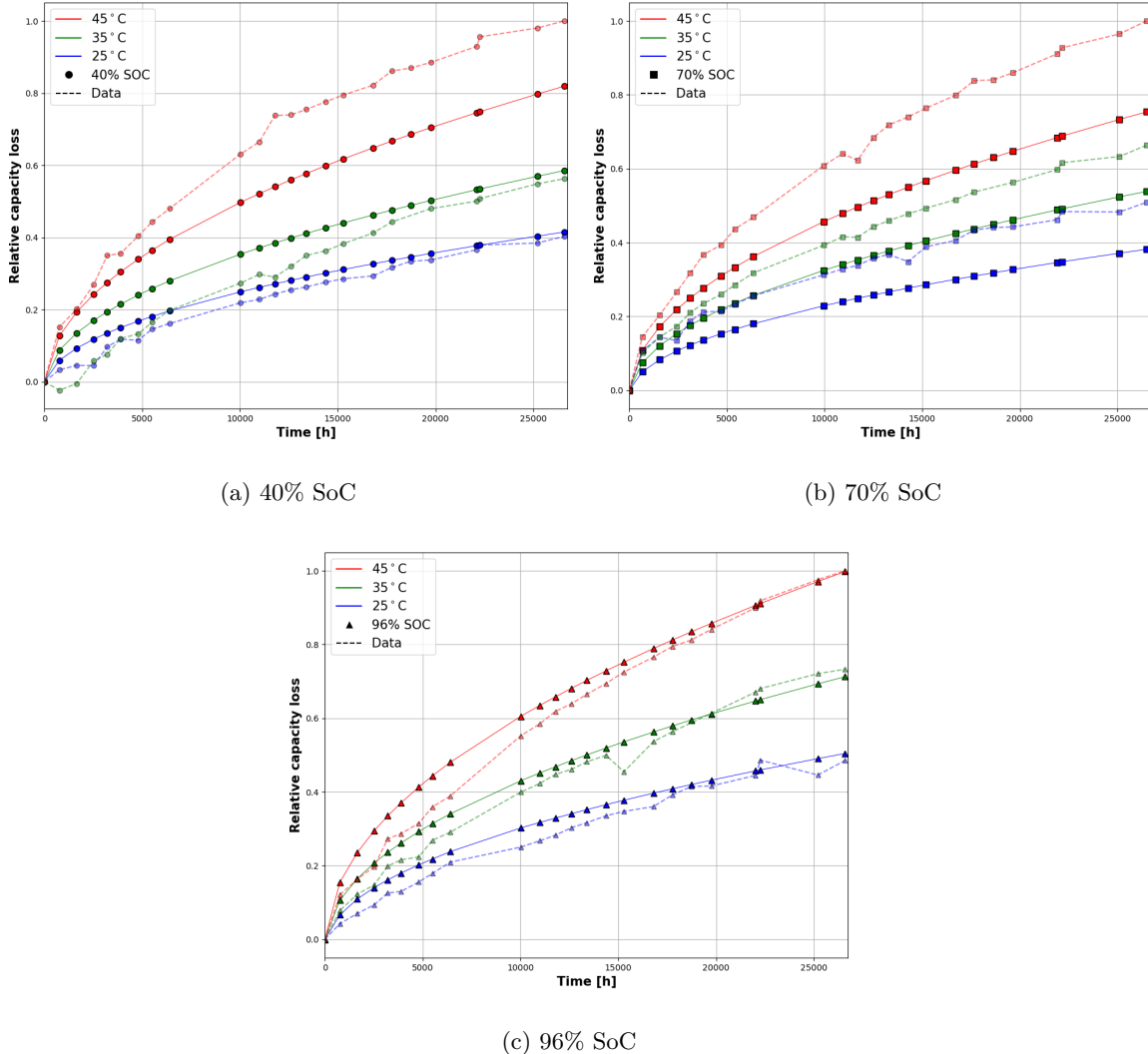


Figure 16: Relative solvent-diffusion limited DFN model between 0 and 1 with only temperature dependency of the inner SEI lithium interstitial diffusivity parameter gathered from Figure 14.

From Figure 15 and 16 it can be observed that the model outputs from PyBaMM fits the experimental data for 96% SoC accurately for all temperatures. The case for 40% SoC shows a good model fit against the experimental data at 25 and 35°C , but a much less accurate fit at 45°C. Lastly, the model fit is not accurate at any temperature for the case of 70% SoC. Arrhenius relations in Figure 12 and 13 for the cell stored at 70% SoC, confirms previous scientific studies' results that the highest rate of capacity degradation of certain LIB chemistries do not occur at the highest SoC levels. This strengthens the hypothesis that an additional cell degradation mechanism such as singlet oxygen evolution introduced in Section 2.1.4 could be more predominant for the cell stored at 70% SoC which is not included in the model. Where additional capacity loss and loss of lithium inventory can be related to the irreversible formation of lithium oxalate. Moreover, the spoon profile behavior seems to be more affected by lower SoC levels as the temperature increases which can be seen in Figure 15 and 16, the same type

of behavior pattern has been identified in previous studies on NMC811/C<sub>6</sub> electrode configuration. To fully measure the dispersion between the model output and the experimental data, the standard deviation was calculated for each temperature and SoC level which can be seen in Table 8.

Table 8: Relative standard deviation between 0 and 1 of the model output and experimental data at all temperatures and SoC levels

| <b>Interstitial-diffusion limited DFN model</b> | <b>25°C</b>  | <b>35°C</b>  | <b>45°C</b>  |
|---|--------------|--------------|--------------|
| <b>40% SoC</b>                                  | 0.009        | 1.00         | 0.609        |
| <b>70% SoC</b>                                  | 0.242        | 0.174        | 0.939        |
| <b>96% SoC</b>                                  | 0.00         | 0.001        | 0.025        |
| <b>Solvent-diffusion limited DFN model</b>      | <b>25 °C</b> | <b>35 °C</b> | <b>45 °C</b> |
| <b>40% SoC</b>                                  | 0.005        | 1.00         | 0.586        |
| <b>70% SoC</b>                                  | 0.267        | 0.185        | 0.901        |
| <b>96% SoC</b>                                  | 0.00         | 0.003        | 0.029        |

As can be seen in Table 8, the standard deviation reaches the highest value at 40% SoC and 35°C. This can have multiple reasons for its occurrence, one of the reasons is that the data includes a lot of noise. Hence, the capacity loss has a negative value in the earlier stages of ageing seen in Figure 15a and 16a which contributes to a large dispersion towards the experimental data. However, the models are able to capture the long-term capacity loss prediction, and the dispersion is mostly concentrated for data points where  $t < 15000$  h. Another reason for the high dispersion is that the SoC calculation in PyBaMM fails at adapting to the slow decrease in capacity under those conditions. Moreover, in order to account for such errors the OCV can be experimentally measured as the cell degrades and lithium is lost to SEI formation, which in theory should result in a more accurate definition of the change in electrode SoC.

### 4.3 Calendar Ageing Model Comparison & Validation

According to the overall results gathered in Section 4.2 both the interstitial-diffusion limited and solvent-diffusion limited DFN models shows promising capabilities to model SEI growth. Furthermore, the solvent-diffusion model seems to be the most promising rate-limiting assumption to apply according to the standard deviations listed in Table 8. However, it is uttermost important to validate models that have generated a good fit to identify that physical and electrochemical parameter can be identified and a dependence on those parameters can be confirmed. To illustrate this a non-identifiable model can fit rather well to the experimental data as can be seen in Figure 17, while not being able to capture the reality of the physical meaning of the data.

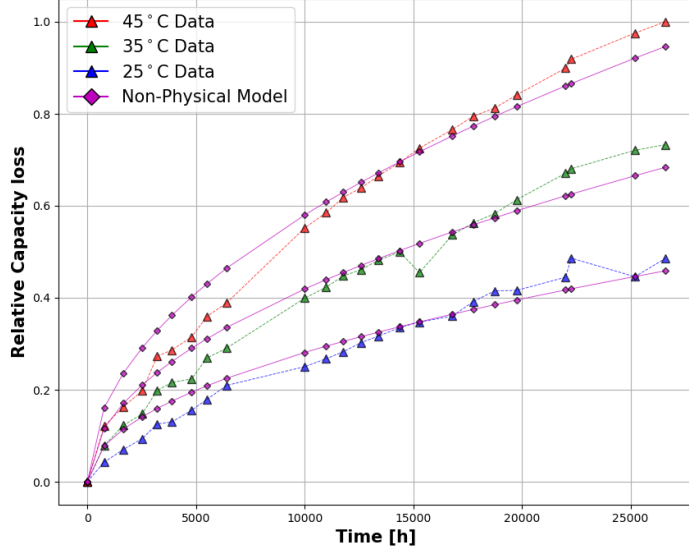


Figure 17: Relative non-physical model between 0 and 1 with  $\sqrt{t}$  dependency fit against experimental data at 96% SoC.

Furthermore, a mathematical model with good fit to experimental data does not necessarily correlate that a model is accurate and representative which can be seen in Figure 17. Hence, the parameter dependency must be verified for each model to ensure that the PyBaMM output is representative in relation to the experimental data. In order to show such dependency, the various different model outputs generated in PyBaMM can be utilized as outlined in Section 2.4.3 to determine if the models are identifiable. From the results presented in Section 4.1 and 4.2, it is clear that cell degradation due to SEI growth is dependent on SoC, and as the cell degrades the SEI layer thickens and the capacity loss gradient decreases. Therefore, the thickness of the SEI layer over time should have a SoC dependency. The simulation results from sweeping the SoC level between 10 - 90% to show the parameter dependency can be seen in Figure 18.

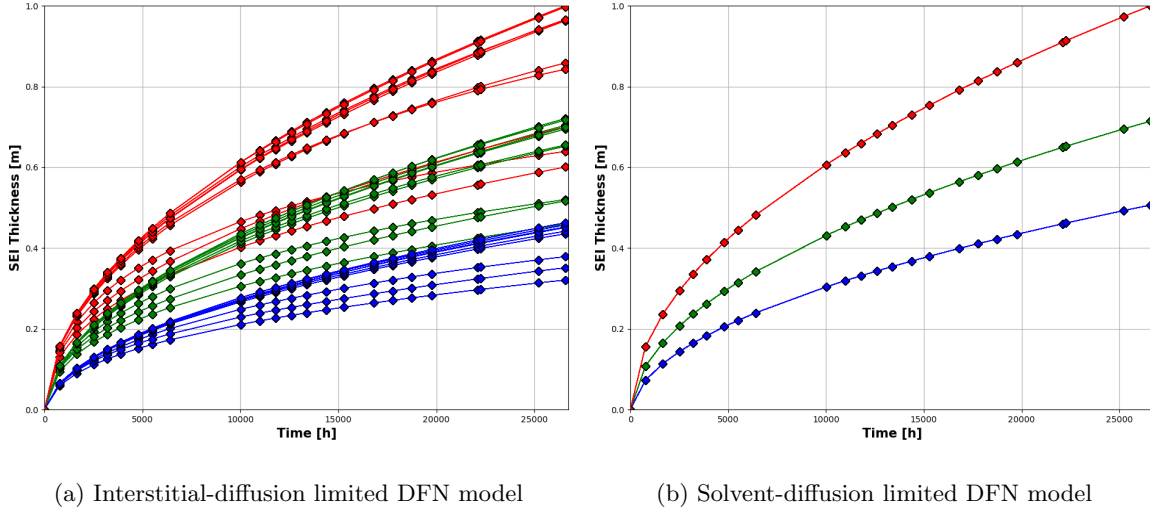


Figure 18: Relative SEI thickness between 0 and 1 as a function of time while sweeping SoC between 10% and 90%

From the result presented in Figure 18, the interstitial-diffusion limited DFN model shows a clear SoC dependence while the solvent diffusion limited DFN model shows none. The solvent-diffusion model does not account for the difference in SEI growth for different SoC levels. The model instead mathematically adjust the output in order to achieve as good fit as possible, which leads the model to be non-identifiable and does not represent the experimental data. Furthermore, the interstitial-diffusion limited DFN model is the only model that is identifiable, and the only model that can represent the data in a physics based model for long term SEI growth.

As the identity of the interstitial-diffusion limited DFN model have been confirmed, PyBaMM was used to simulate and measure the internal resistance of the cell under the whole calendar ageing process with DCIR tests as outlined in Section 3.3.3. Where the SEI thickness and internal resistance of the cell can was analyzed as a function of time for the different temperatures and SoC levels. The results from the DCIR tests for both discharge and charge pulses for 40% SoC at 25°C in PyBaMM can be seen in Figure 19.

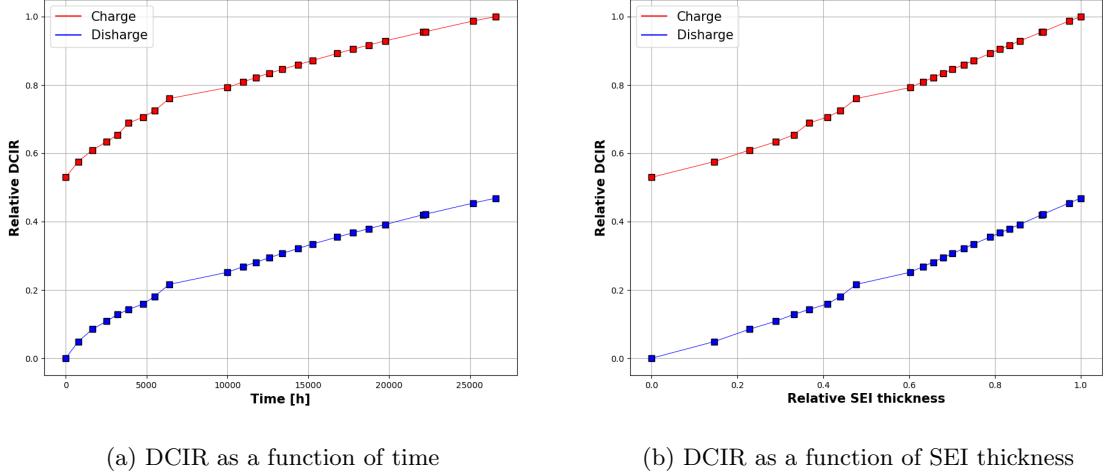
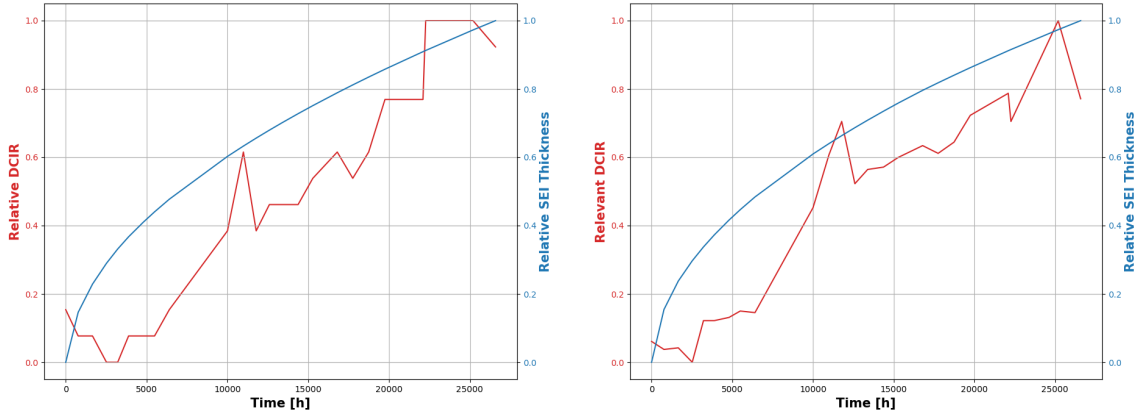


Figure 19: Relative charge and discharge DCIR between 0 and 1 simulations for interstitial-diffusion limited DFN model at 40% SoC and 25 °C.

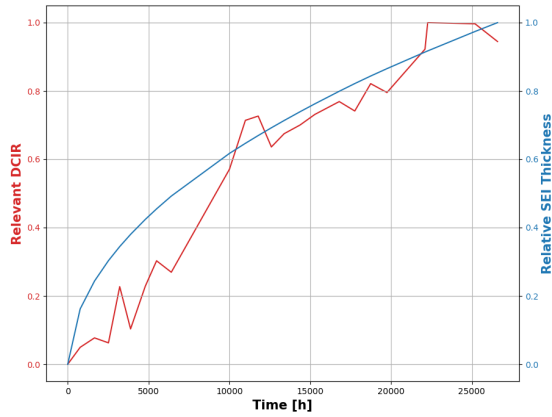
From Figure 19b it is evident that the DCIR increases almost linearly with the thickness of the SEI layer. Which in theory make sense, since the resistance should increase as the layer thickens due to a increased potential difference over the SEI layer. Furthermore, the DCIR follows the same  $\sqrt{t}$  dependency as SEI growth and interstitial-diffusion limited DFN which can be seen in Figure 19a. Moreover, since the results from Figure 19a shows the same time dependency, SEI is most exclusively the predominate resistance source within the cell. Which in retrospect is not fundamentally correct according to the real world since the model implemented only considers SEI growth as a degradation mechanism. The results also provide evidence that the interstitial-diffusion limited DFN model can capture the increase of resistance as the thickness of the SEI increase. Furthermore, the results from the validation process of the DFN model, shows important results in capturing the physics behind the data in physics-based battery degradation modelling of SEI growth, which could be combined with additional degradation mechanisms in order to understand degradation process and the interaction effect between different mechanisms more thoroughly.

An example of achieving better understanding of the accuracy of DCIR simulations shown in Figure 19 is to compare the modelling results against experimental measurements of DCIR as can be seen in Figure 20. Which as previously mentioned, does not only capture SEI growth as the only source of increased resistance but rather the overall internal resistance of combined degradation mechanisms at different conditions. The DCIR data measurements shown in Figure 20 were conducted at temperatures of 25, 35, and 45 °C and the data was supplied by the manufacturer of the battery cells.



(a) DCIR data and SEI thickness at 25 °C

(b) DCIR data and SEI thickness at 35 °C



(c) DCIR data and SEI thickness at 45 °C

Figure 20: Relative DCIR between 0 and 1 from experimental data acquired from the battery supplier, compared to PyBaMM model output of the SEI thickness over time at different temperatures and 40% SoC

From Figure 20 it can be seen that the DCIR follows a more  $\sqrt{t}$  dependency as the temperature of the cell increases during the ageing process. Hence, the internal resistance from the growth of SEI becomes more predominant as the temperature of the cell increases, which is characterized by the more evident dependency of  $\sqrt{t}$ . While at lower temperatures the SEI resistance is not as predominant, and the resistance from alternative components within the cell or measuring equipment is a more dominant source of resistance. This connects the relation between the DCIR and the growth rate of SEI increases with temperature and peaks at 70% SoC from the experimental data, which can be seen in Figure 18a for the interstitial-diffusion limited DFN model. However, previous results that are shown in Section 4.2 showed signs of additional cell degradation mechanisms, more specifically the shuttle reaction which further accelerates the ageing process at 70% SoC and 40% SoC for high temperatures. Hence, this should also be identifiable in DCIR measurements where the contribution of resistance from the SEI layer should not be that predominant under those conditions where the shuttle reaction is assumed to occur. A comparison between relative DCIR measurement values at previously studied SoC and temperatures conditions can be seen in Table 9.

Table 9: Relative DCIR measurements values between 0 and 1 from the battery supplier under different conditions after 1000 days of storage.

| Storage Conditions | 25 °C | 35 °C | 45 °C |
|--------------------|-------|-------|-------|
| 40% SoC            | 0.00  | 0.028 | 0.125 |
| 70% SoC            | 0.013 | 0.064 | 0.127 |
| 96% SoC            | 0.149 | 0.505 | 1.00  |

From Table 9 it is evident that the cell achieves the highest values of DCIR measurements at storage conditions of 96% SoC. Furthermore, 70% SoC storage cell experiences the least amount of increased DCIR over the different temperatures, while simultaneously being the cell that degrades at the highest rate. This shows evidence that the SEI layer is not the dominant degradation mechanism under those conditions and that the cell represented in experimental data for 70% SoC in Figure 9 is subject to alternative sources of degradation and lithium depletion within the cell. Similar behavior can also be identified for the 40% SoC cell, where the relative value of DCIR is within the same proximity as the 70% SoC, which also shows evidence of an additional dominant cell ageing mechanism at lower SoC levels and higher temperatures.

#### 4.4 Cycling Ageing with SEI & Lithium Plating

From the previous results in Section 4.4, the results showed that the interstitial-diffusion DFN model is the most accurate rate-limiting assumption to apply in order to capture the physics behind long-term SEI growth in calendar ageing. In the following section the results from the optimized SEI model with a connected irreversible lithium plating model introduced in Section 2.1.2 and 2.1.3. The cycling data acquired from a long term test that was used to fit the model can be seen in Figure 21, which was gathered from identical charging protocols to the ones which can be observed in Table 2.

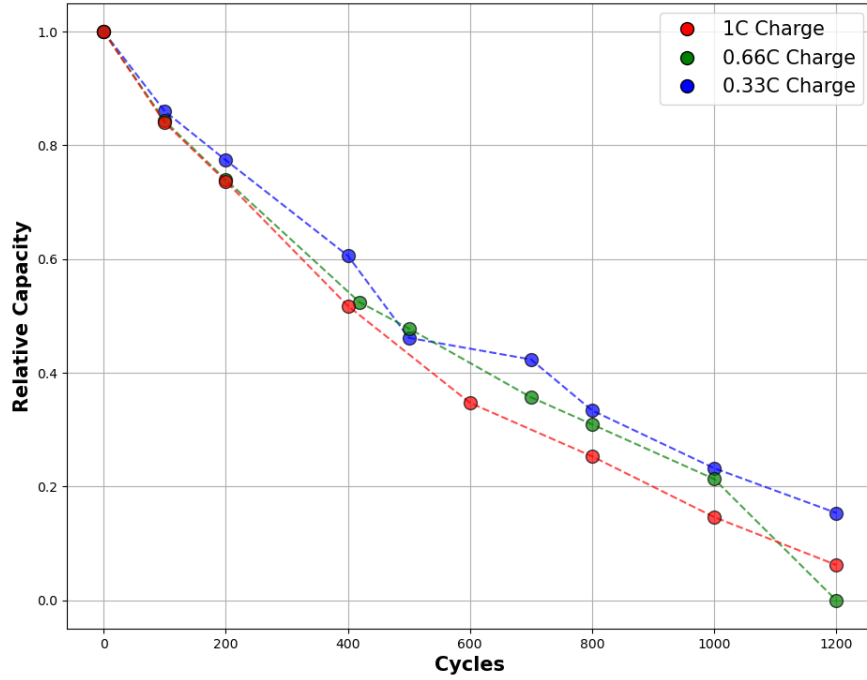


Figure 21: Relative capacity between 0 and 1 as a function of cycles obtained from battery supplier under three different charging protocol which can be seen in Table 2.

From Figure 21 it can be observed that with increased C-rate the rate of cell degradation increases, with an outlier being the data point for 0.66 C at 1200 cycles. This data point's sudden drop in capacity is considered to be caused by noise from the experimental measurement equipment, hence assuming 1.00 C shows the highest rate of cell degradation over the 1200 cycles. It can also be observed that the highest rate of degradation occurs at the beginning of cycling, which is similar to the behavior that could be observed from the data of calendar ageing experiments shown in Figure 9. This characteristic  $\sqrt{t}$  dependency is connected to the high rate of SEI formation at the initial stages of cell ageing, which over time decreases until lithium plating is the more predominant cell degradation mechanism with a linear capacity fade. A similar approach to the parameter estimation outlined in Section 3.3.2 the parameters for the irreversible lithium plating that are shown in Appendix A.3.7 were identified. Furthermore, the only affecting parameter that could be isolated with the numerical methods described in Section 2.4.2 was the lithium plating rate constant, which is evidently part of the Butler-Volmer expression for lithium plating presented in (16). A parameter sweep of the lithium plating rate constant for the three different experimental protocols shown in Table 2 and in relation to experimental data in Figure 21 can be seen in Figure 22.

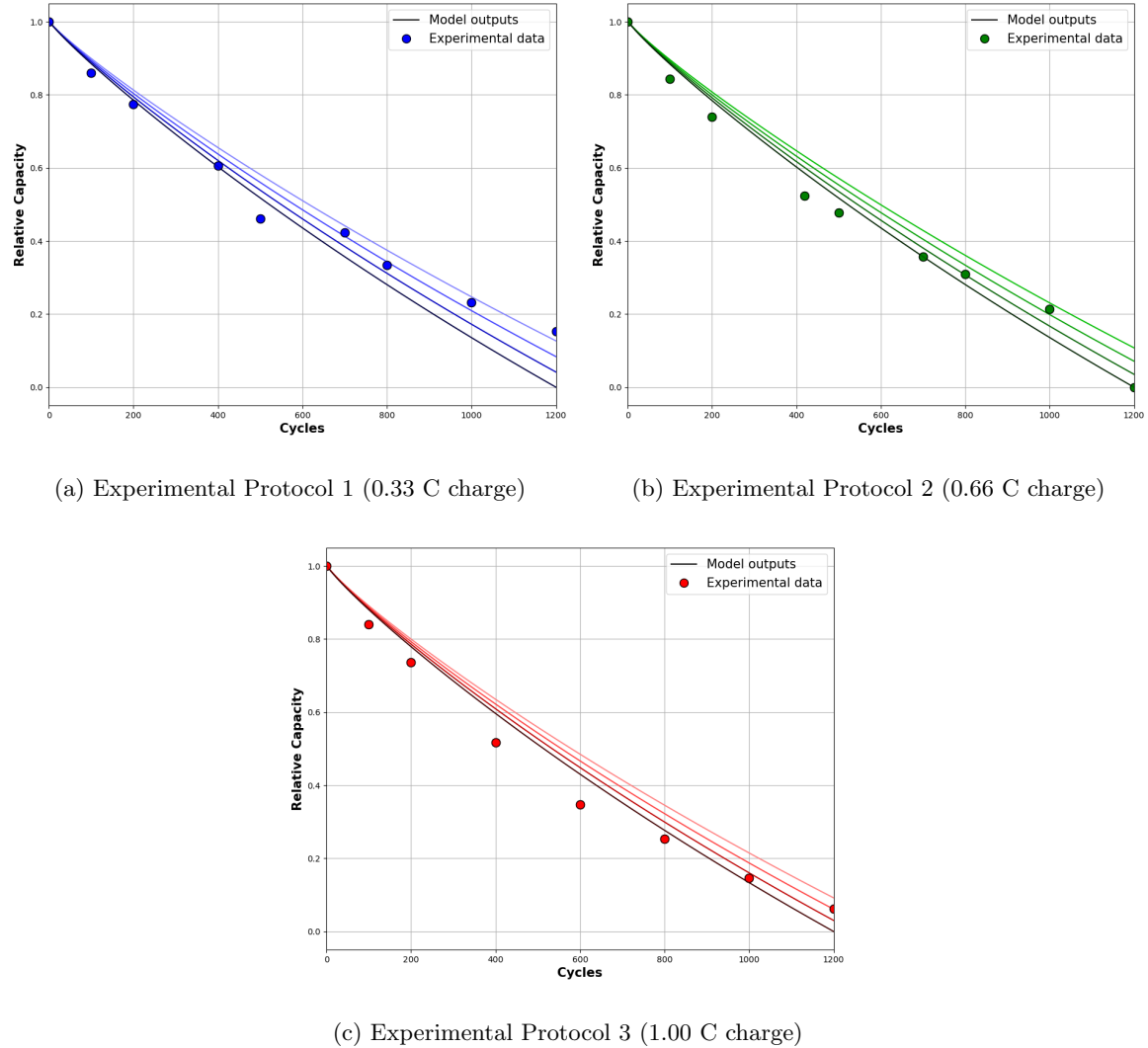


Figure 22: Relative parameter sweep of the lithium plating kinetic rate constant parameter between 0 and 1 against the experimental data in Figure 21 for each protocol.

From the results shown in Figure 22 it can be seen that the relative capacity reduces with increased C-rate during the charging process. Furthermore, the results from the 1 C charging which can be seen in Figure 22c present a rapid initial degradation process compared to the case of 0.33 C shown in Figure 22a. This could be due to additional degradation mechanisms such as surface cracking which is outlined in Section 2.1.5. An increase in C-rate results in a higher rate of intercalation and extraction process of  $\text{Li}^+$  in the anode. This potentially can lead to the anode cracking and exposing the naked surface to the electrolyte, which bolsters the capacity losses to additional SEI formation. A summary of the relative parameter sweep interval of lithium plating kinetic rate constant used to generate the results in Figure 22 can be viewed in Table 10.

Table 10: Relative values between 0 and 1 of the results acquired from the rough estimation sweep of the lithium plating kinetic rate constant parameter in PyBaMM visualized in Figure 22.

| <b>Experiment</b> | <b>Lower limit</b> | <b>Upper limit</b> | <b>Optimal value</b> | <b>Standard deviation</b> |
|-------------------|--------------------|--------------------|----------------------|---------------------------|
| <b>Protocol 1</b> | 0                  | 0.33               | 0                    | 0.38                      |
| <b>Protocol 2</b> | 0.33               | 0.66               | 0.55                 | 0                         |
| <b>Protocol 3</b> | 0.66               | 1.00               | 0.78                 | 1.00                      |

From Table 10 it can be observed that the kinetic reaction constant for lithium plating increases with C-rate during charging. Where increased charging C-rate can be directly correlated to a larger amount of plated lithium and further increased capacity losses as seen in the relation shown in (12) and (13). The most optimal values of the kinetic rate constants were roughly estimated by comparing the model output against the experimental data and evaluating the standard deviation. Optimal values of the kinetic rate constants were chosen based on the model output with the least deviation against the experimental data also displayed in Table 10. PyBaMM's versatile variable output was utilized to gain more knowledge about how much SEI and lithium plating contribute to the ageing of the cell which can be seen visualized in Figure 23.

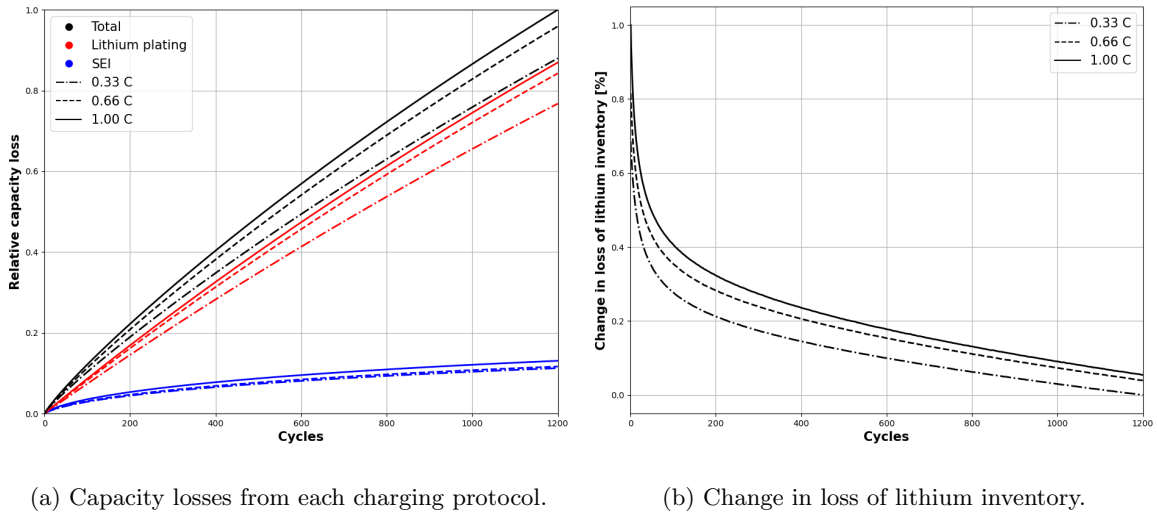
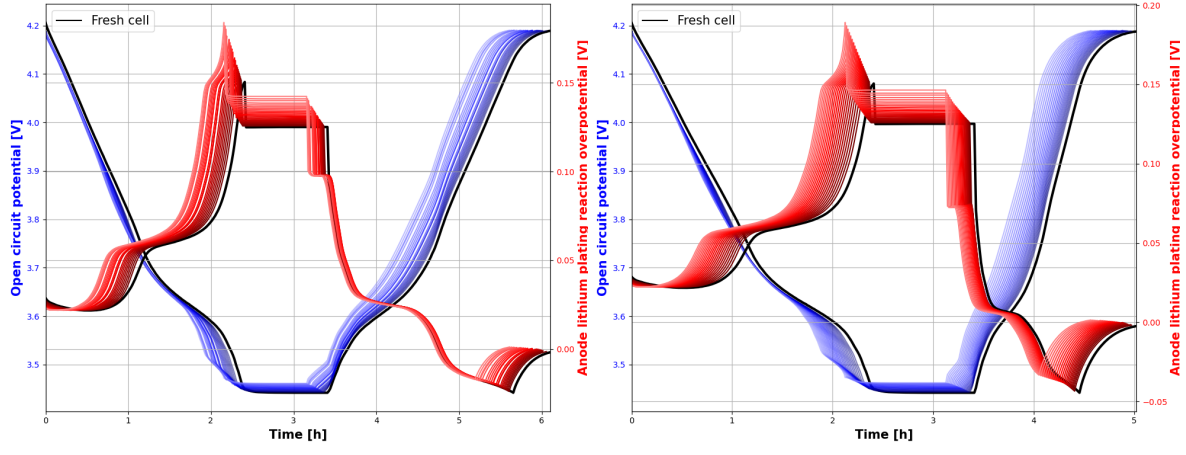
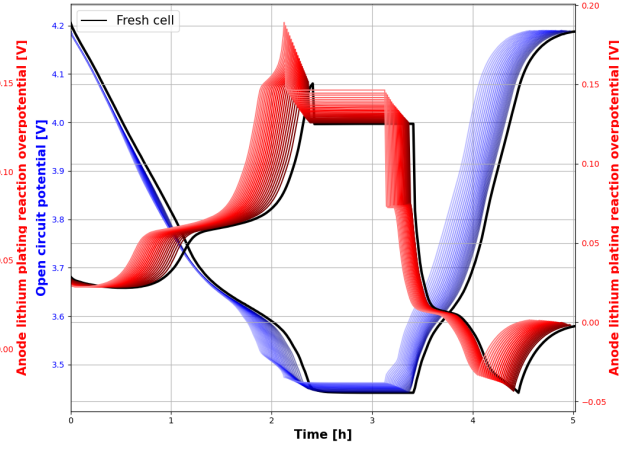


Figure 23: Relative capacity losses between 0 and 1 for each degradation mechanism and total capacity losses of the cell, with percentage of lost lithium inventory for every cycle of the experiment as a comparison.

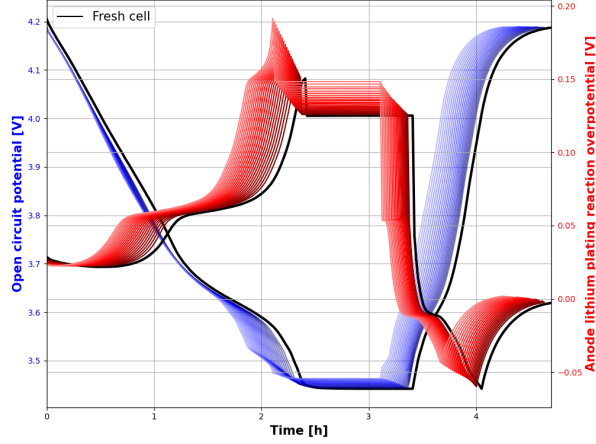
From Figure 23 it can be observed that the highest rate of degradation occurs at the earlier stages of cycling. Which is due to a large amount of SEI formation with the clear characteristic  $\sqrt{t}$  dependency which stabilizes after around 400 cycles and transitions over to linear dependency for the change in loss of lithium inventory per cycle resulting in a continuously decreasing degradation which can be seen in Figure 23b. Furthermore, the loss of capacity to SEI formation over 1200 cycles ranges between  $\sim 12.8 - 13.1\%$  of the total capacity loss of the cell, while lithium plating contributes to  $\sim 86.9 - 87.2\%$  of the total capacity loss of the cell for each charging protocol. The rate of degradation increases with higher C-rate over the 1200 cycles, where the capacity losses to SEI and lithium plating increase as can be seen in Figure 23a. The difference in loss of lithium inventory for each cycle between the charging protocols shown in Figure 23b is getting smaller for each cycle. This might be due to the exclusion of implementing various mechanical degradation mechanisms such as surface cracking described in Section 2.1.5 that are more predominant for cells exposed to higher C-rates. Moreover, a cell subjected to a protocol with a higher charging C-rate will deplete more of its lithium inventory to SEI formation and lithium plating in the earlier stages of ageing. Since no new electrode surface will be exposed if mechanical stress is not included, making the distance for diffusion larger and larger at the negative electrode. This will eventually lead to the two degradation mechanisms' formation rates will decrease over time. Where a higher C-rate shows that the decrease in the rate of formation of SEI and plated lithium will occur earlier in the ageing process and at a higher rate, which can be observed in Figure 23b. Hence, the behavior that can be observed in Figure 23b is most likely due to the the assumptions and delimitations made to the model in the project. To be able to further investigate the ageing process of the cell, the relation between the cell OCV in respect to SoC outlined in Section 2.2 and the lithium plating reaction overpotential in Section 2.1.2 - 2.1.3 was visualized for each 50th cycle as can be seen in Figure 24.



(a) Experimental Protocol 1 (0.33 C charge)



(b) Experimental Protocol 2 (0.66 C charge)



(c) Experimental Protocol 3 (1.00 C charge)

Figure 24: Cell OCV in relation to lithium plating reaction overpotential for each 50th cycle, where the black line represents a fresh cell, and a lighter fading color represents later stages of the cycling experiment

The most evident difference in the results from the three charging protocols visualized in Figure 24 is the behavior of the lithium plating overpotential after 3 hours where charging of the cell occurs at different C-rates. It can be observed that the drop of the lithium plating overpotential increases and reaches lower negative values with an increased charging current, amplifying the rate of formation of plated lithium and increasing the rate of cell degradation. However, it can also be observed that the difference in lithium plating overpotential in relation to the fresh cell at all stages of the cycle increases with the C-rate, especially during the charging stage throughout the ageing process. This behavior can be correlated to the results that were previously presented in Figure 24b where the ageing process is hindered due to no mechanical stress being applied to expose additional electrode surface to the electrolyte, which reduces the rate of cell degradation even though in reality it should increase. Furthermore, the porosity of the SEI layer has throughout the project been assumed to be constant, while in reality, it changes during the ageing process promoting additional lithium plating and non-linear ageing due to less accessible pores and reduced anode ionic kinetics as previously described in Section 2.1.2. A summary of the difference between the lowest value of the lithium plating reaction overpotential, and the time difference between the cell is subjected to negative values of the lithium plating reaction overpotential for the initial and 1200th cycle can be seen in Table 11. A visualization for each 50th cycle when the cell is subjected to negative values of the lithium plating reaction overpotential can be seen Figure 32 in Appendix A.1.

Table 11: Summary of difference of time spent at negative lithium plating reaction overpotential and the difference in the lowest value of the lithium plating overpotential between the initial and the 1200th cycle.

| Charging Current | $\Delta t \eta_{\text{Li}} < 0$ [h] | $\Delta \eta_{\text{Li}}$ [V] |
|------------------|-------------------------------------|-------------------------------|
| 0.33C            | 0.573                               | 0.008                         |
| 0.66C            | 0.410                               | 0.011                         |
| 1C               | 0.367                               | 0.018                         |

As can be seen from the summary presented in Table 11 the time spent at negative values of lithium plating reaction overpotential decreases with lower values of C-rates. While the lowest output value of the lithium plating reaction decreases with higher values of C-rates. After an arbitrary number of cycles, the translated loss of lithium inventory for each cycle will converge to the same amount for all protocols. Which is heavily influenced by the time spent at negative values but also the lowest value of the lithium plating reaction overpotential presented in Table 11 and Figure 32 in Appendix A.1. Hence, explaining the converging effect between the charging protocols in terms of loss of change in loss of lithium inventory as the cycle number is increasing presented in Figure 23b. This as previously discussed is probably due to the absence of implementing mechanical stress and changes of the SEI porosity and should be taken into consideration when evaluating the effects that both lithium plating and SEI have on the degradation. To further investigate the effect SEI and lithium plating have on the cell degradation, both the negative and positive electrode OCV obtained from the model are visualized and compared for each 50th cycle in Figure 25.

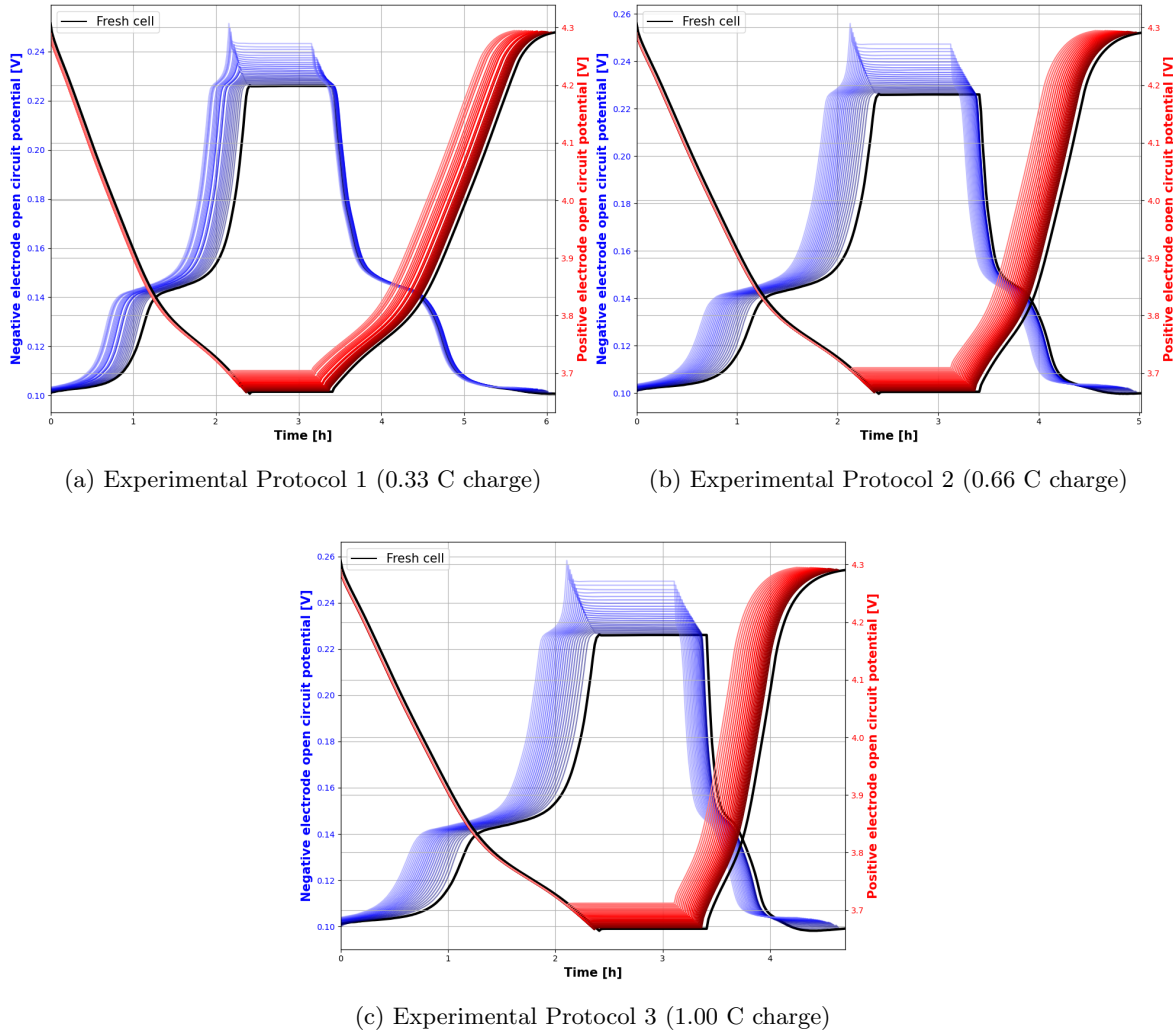


Figure 25: Electrode OCV in relation to each other for each 50th cycle, where the black line represents a fresh cell, and a lighter fading color represents later stages of the cycling experiment

From the results shown in Figure 25 it can be observed that the factor contributing the most to the difference in the overall cell OCV during the ageing process shown in Figure 32 is the negative electrode OCV. While the difference in the positive electrode OCV is relatively identical for all charging protocols, with the exception that a cycle is conducted under a shorter timeframe with higher charging C-rate. This aligns with the theory of SEI formation and lithium plating outlined in Sections 2.1.1 - 2.1.3, where the degradation mechanisms implemented are parasitic reactions to the intercalation process of  $\text{Li}^+$  in the negative electrode during the charging process. Two of the three conditions where lithium plating is significantly increased are showcased in Figure 4 can be analyzed by modeling the experimental protocols, more specifically high C-rates and high SoC levels. Where both conditions cause a larger concentration of  $\text{Li}^+$  to accumulate at the interphase of the negative electrode due to rate-limiting solid-phase diffusion of the intercalation process at high C-rates, or a small amount of available active sites for the intercalation can take place at high SoC levels. Furthermore, the largest observable sign of increased cell ageing of the negative electrode is the shift of OCV during the charging process with increased C-rate and higher SoC levels, which are achieved in the later stages of the cycling process in Figure 25. To be able to evaluate the effect the ageing process has had on the negative electrode, the negative electrode OCV at the last data point of the rest period at constant voltage and 100% SoC was analyzed which can be seen in Figure 26.

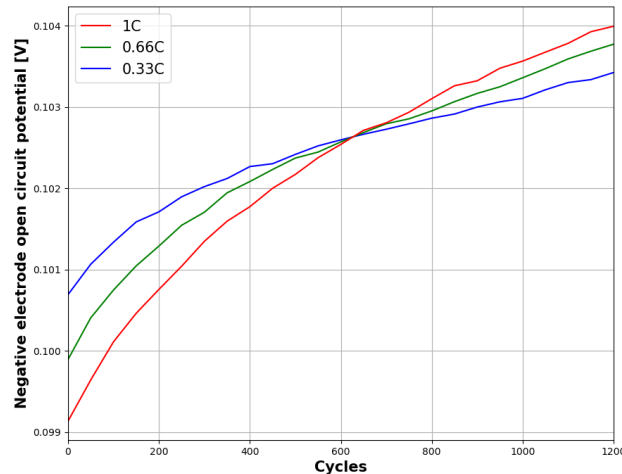


Figure 26: Negative electrode OCV as a function of cycle number over the ageing process for each charging protocol of the last data point at 100% SoC

The evolution for the negative electrode OCV at 100% SoC during the ageing process shows that the cell exposed to a higher C-rate achieves a higher  $\Delta\text{OCV}$ , which can be observed in Figure 26. By analyzing the last data point while the cell is held constant voltage at 100% SoC we can retrieve information on how the maximum amount of intercalated lithium ions are affected by the continuous degradation caused by SEI and lithium plating according to (18). Hence, a larger value of  $\Delta\text{OCV}$  at 100% SoC suggests that the cell has lost more of its capability to facilitate the lithium ions in the intercalation process, thus reducing the cell capacity. To further explore the effect of the loss of lithium inventory and the capability of intercalating lithium ions has had on the capacity of the cell, the electrode capacities as a function of the cycling number are visualized in Figure 27.

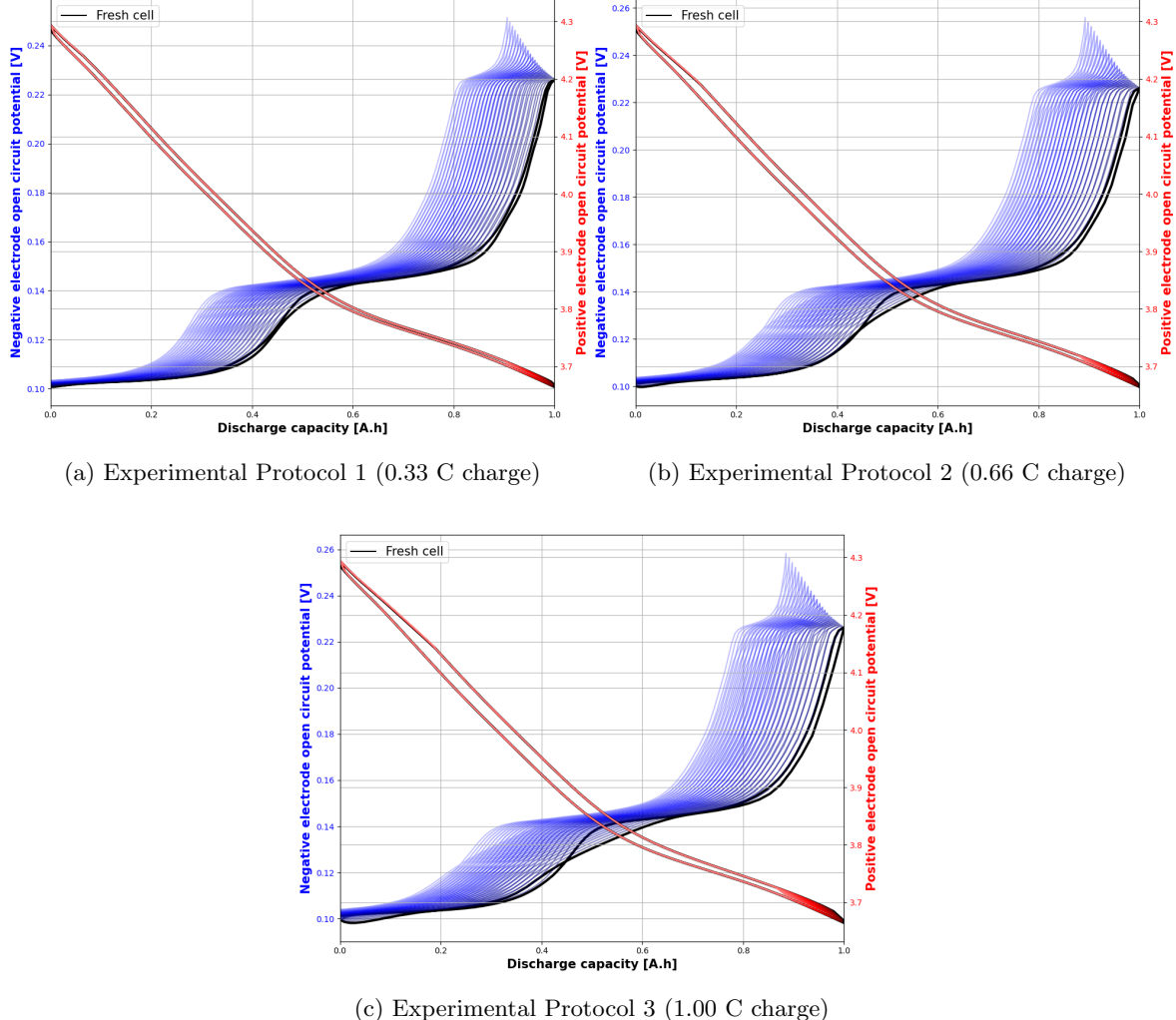


Figure 27: Electrode OCV as a function of the relative discharge capacity between 0 and 1 of the cell for each 50th cycle. Where the discharge capacity is the time integral of the current during the experimental protocol.

From Figure 27 the OCV for negative and positive electrodes during charge and discharge can be observed. Furthermore, a distinct characteristic of the result is that the negative electrode is the only electrode that shows signs of degradation in terms of capacity losses, which aligns with the results previously presented in Figure 25 and 26. The results root back to the assumptions that have been applied to the model, while in a perfect world the positive electrode OCV should also be affected by various degradation mechanisms. While only considering SEI and lithium plating as cell degradation mechanisms the only signs of degradation can be observed at the negative electrode. Hence, to be able to capture a more realistic degradation process of battery cycling ageing with a physical model additional mechanisms must be added, and the interaction effect between those mechanisms must be properly defined.

However, when only analyzing SEI growth and lithium plating the DFN model created in PyBaMM captures the physics of cell degradation while also being identifiable. This has previously been shown for the interstitial-diffusion limited SEI growth in Section 4.3, but can also be determined for the additional implemented irreversible lithium plating model. Hence, the results generated by the model in this section confirm the theory in Section 2.1.2 that the amount of plated lithium is significantly increased during charging with higher C-rates and high levels of SoC. Additionally, the SEI growth and lithium plating mechanisms get hindered by themselves over time as the number of cycles is increased, which corresponds to the theory behind the two degradations mechanisms in Section 2.1.1 - 2.1.3 and the governing equations the change in overpotential shown in (7) and (13). The loss of lithium inventory results in Figure 23b correspond to the  $\Delta$ OCV which increases with the C-rate and reduces the capacity of intercalated lithium ions in the negative electrode. Thus, the model is giving an output that only shows a capacity loss in the negative electrode which constitutes the whole LIB cells capacity loss.

## 5 Conclusion

In the following sections the conclusions that can be drawn from the results of the project be presented. Where the sections are split up into two main sections. The first section will cover the conclusions of the calendar ageing process of the LIB cell, where the focus was to isolate and estimate affecting parameters connected to SEI growth. The second section will cover the conclusions that can be drawn from the cycling ageing process, where lithium plating was implemented and optimized alongside the optimized SEI model. The physics-based model and the PyBaMM framework have made it able not only to analyze the data but also to quantify and observe the effects degradation mechanisms have on an electrochemical system. Hence, provide valuable information to R&D engineers to increase the lifetime and reduce the development cost but most importantly increase the lifetime and reduce the environmental impact of EVs.

### 5.1 Calendar Ageing

The assessment covering the topic of modeling calendar ageing found that the LIB cell degrades at a higher rate during storage with increased temperature. While showing the highest degradation rate occurs at 70% SoC for each temperature condition investigated in this project which can be observed in Figure 9. The most optimal rate-limiting assumption to apply for modelling SEI growth for calendar ageing at different temperatures and SoC levels are the interstitial-diffusion model, due to its capability of capturing the potential and SoC dependencies throughout the ageing process. Hence, capturing the physics behind SEI growth at different conditions of the calendar ageing process. SEI growth is the most predominant cell ageing mechanism during storage, and is therefore suitable for calibrating, parameterizing, and validating SEI models.

The only affecting parameter for the interstitial-diffusion model in PyBaMM for SEI growth was the “Inner SEI lithium interstitial diffusivity”, where the most suitable average value of the affecting parameter was obtained through an Arrhenius relation. Furthermore, the Arrhenius relation also provided valuable results in form of activation energies at different conditions of the calendar ageing. The Arrhenius relation was also essential for the detection of the anomalies in the activation energies and capacity degradation for 40% SoC at high temperatures, and 70% SoC at all temperatures observed in Figure 13. The detected anomaly has the scientific research recently been able to link to singlet oxygen evolution occurring at the cathode surface for NMC LIBs at certain SoC intervals, see Section 2.1.4.

The anomalies in activation energies and capacity degradation for 40% SoC at high temperatures, and 70 % at all temperatures were further analyzed and investigated with DCIR. Which showed that the internal resistance for the cell stored at 70% SoC was, in fact, the lowest, suggesting that an additional ageing mechanism apart from SEI is present which does not contribute to increasing resistance build-up. The slow increase of resistance build-up as a function of temperature for the cell stored at 40 % SoC suggests that the cell is subjected to similar additional ageing mechanisms as the cell stored at 70% SoC. Moreover, the increased rate of degradation concept referred to as the “spoon profile” behavior seems to be more influenced by lower than higher SoC levels when the temperature increases.

### 5.2 Cycling Ageing

The cycling assessment introduced the implementation of lithium plating mechanisms along with the optimized SEI model. Similar to the calendar ageing, lithium plating only had one affecting parameter

“lithium plating kinetic rate constant” and was roughly estimated by sweeping an interval of values and fitting it against experimental data. The rate of cell degradation increased with increased C-rate, while for all cases capacity loss due to the lithium plating mechanism constituted almost 90% of the total capacity losses.

The three different charging protocols showed a rapid decrease in capacity during the initial cycles of the ageing process, where the rate of cell degradation decreased over time and cycle number. Which is caused by the continuous depletion of the cell’s lithium inventory and excessive SEI growth. This over an arbitrary amount of cycles will lead to a converging effect in the change in the loss of lithium inventory between the three chagrining protocols which can be seen in Figure 23b. Where this behavior is due to the absence of mechanical degradation mechanisms such as particle cracking. This would have included modelling of exposing new electrode surface to the electrolyte and further accelerating the degradation process of the cell, especially for cells subjected to increased C-rate.

Furthermore, the cycling was also able to capture electrochemistry behind the capacity loss, which includes the loss of lithium inventory to irreversible SEI and lithium plating, but also the change in intercalated lithium capacity in the negative electrode during charging. Where an increased  $\Delta\text{OCV}$  value could be observed with increased C-rate during the ageing process which is a clear indication of increased cell degradation.

## 6 Future Work

For future work which would increase the information that can be obtained from physics-based models in PyBaMM to be able to explain the degradation more in detail some of the following sections can be considered:

The change in activation energy and increased rate of degradation for the cell stored at 70 % SoC needs to be investigated. Moreover, go further into the concept of singlet oxygen evolution and gas evolution outlined in Section 2.1.4 in order to quantify the capacity lost to gas evolution in NMC LIBs. Which will increase the accuracy of future physics-based battery models.

Issue more in-house experiments at more SoC levels for the calendar ageing process. This would provide more information about the “spoon profile” for the selected electrode composition, but also valuable information on how embedded systems in EV should react under specific conditions. To reduce and mitigate LIB degradation when idle for a longer period.

Analyze the cycling ageing process for the cell while cycling between different SoC intervals. For instance, cycling between 10 – 90%, 20 – 80% and 30 – 70% SoC. This would provide more information about the effects of the accelerated lithium plating process at high SoC values and negative values of  $\eta_{Li}$ , which would be a great asset to fit the physics-based model against.

Conduct differential voltage analysis throughout the ageing process both for calendar and cycling ageing which the model and parameter can be fit against. This would provide more valuable information regarding the loss of lithium inventory and the loss of electrode capacities and degradation. Hence, also outline the effect that the positive electrode has on the overall cell degradation which is non-existing the in current model as seen in Figure 27.

Implement mechanical degradation mechanisms, such as particle cracking into the physics-based model. This will create a more accurate model that will receive a better fit against the experimental data seen in Figure 22. Thus, a more increased rate of degradation would be observed for cells subjected to higher C-rate, and be less limited by the already formed SEI layer since the new electrode surfaces will be exposed to the electrolyte as cracks start to form.

## References

- [1] Michel Armand et al. “Lithium-ion batteries – Current state of the art and anticipated developments”. en. In: *Journal of Power Sources* 479 (Dec. 2020), p. 228708. ISSN: 0378-7753. DOI: 10.1016/j.jpowsour.2020.228708. URL: <https://www.sciencedirect.com/science/article/pii/S0378775320310120> (visited on 01/17/2022).
- [2] Ulrich von Sacken et al. “Comparative thermal stability of carbon intercalation anodes and lithium metal anodes for rechargeable lithium batteries”. en. In: *Solid State Ionics* 69.3 (Aug. 1994), pp. 284–290. ISSN: 0167-2738. DOI: 10.1016/0167-2738(94)90417-0. URL: <https://www.sciencedirect.com/science/article/pii/0167273894904170> (visited on 01/19/2022).
- [3] Reiner Korthauer. *Lithium-Ion Batteries: Basics and Applications*. eng. 1st ed. 2018.. Book Title: Lithium-Ion Batteries: Basics and Applications. Berlin, Heidelberg: Springer Berlin Heidelberg, 2018. ISBN: 978-3-662-53071-9.
- [4] Dongjiang Li et al. “Modeling the SEI-Formation on Graphite Electrodes in LiFePO<sub>4</sub> Batteries”. en. In: *Journal of The Electrochemical Society* 162.6 (Feb. 2015). Publisher: IOP Publishing, A858. ISSN: 1945-7111. DOI: 10.1149/2.0161506jes. URL: <https://iopscience.iop.org/article/10.1149/2.0161506jes/meta> (visited on 01/19/2022).
- [5] Thomas F. Fuller and John N. Harb. *Electrochemical engineering*. eng. Book Title: Electrochemical engineering. Somerset: Wiley, 2018. ISBN: 978-1-119-00425-7.
- [6] Ann Cornell. *F2\_Thermodynamics\_2020.pdf: KE2110 HT20-1 Applied Electrochemistry*. URL: [https://canvas.kth.se/courses/19829/files/3174318?module\\_item\\_id=248150](https://canvas.kth.se/courses/19829/files/3174318?module_item_id=248150) (visited on 01/18/2022).
- [7] Ann Cornell. *F3\_Kinetics\_2020.pdf: KE2110 HT20-1 Applied Electrochemistry*. URL: [https://canvas.kth.se/courses/19829/files/3188182?module\\_item\\_id=250100](https://canvas.kth.se/courses/19829/files/3188182?module_item_id=250100) (visited on 01/19/2022).
- [8] *Greenhouse Gas Emissions from Energy: Overview – Analysis*. en-GB. URL: <https://www.iea.org/reports/greenhouse-gas-emissions-from-energy-overview> (visited on 01/20/2022).
- [9] Meng Yuan et al. “The electrification of transportation in energy transition”. en. In: *Energy* 236 (Dec. 2021), p. 121564. ISSN: 0360-5442. DOI: 10.1016/j.energy.2021.121564. URL: <https://www.sciencedirect.com/science/article/pii/S0360544221018120> (visited on 01/20/2022).
- [10] *Alternative Fuels Data Center: How Do Plug-In Hybrid Electric Cars Work?* URL: <https://afdc.energy.gov/vehicles/how-do-plug-in-hybrid-electric-cars-work> (visited on 01/20/2022).
- [11] *Alternative Fuels Data Center: How Do Hybrid Electric Cars Work?* URL: <https://afdc.energy.gov/vehicles/how-do-hybrid-electric-cars-work> (visited on 01/20/2022).
- [12] *Alternative Fuels Data Center: How Do All-Electric Cars Work?* URL: <https://afdc.energy.gov/vehicles/how-do-all-electric-cars-work> (visited on 01/20/2022).
- [13] Xiao-Guang Yang and Chao-Yang Wang. “Understanding the trilemma of fast charging, energy density and cycle life of lithium-ion batteries”. en. In: *Journal of Power Sources* 402 (2018), pp. 489–498. ISSN: 0378-7753. DOI: 10.1016/j.jpowsour.2018.09.069. URL: <https://www.sciencedirect.com/science/article/pii/S0378775318310462> (visited on 01/20/2022).

- [14] Alana Zülke et al. “High-Energy Nickel-Cobalt-Aluminium Oxide (NCA) Cells on Idle: Anode-versus Cathode-Driven Side Reactions”. en. In: *Batteries & Supercaps* 4.6 (2021). \_eprint: <https://onlinelibrary.wiley.com/doi/pdf/10.1002/batt.202100046>, pp. 934–947. ISSN: 2566-6223. DOI: 10.1002/batt.202100046. URL: <https://onlinelibrary.wiley.com/doi/abs/10.1002/batt.202100046> (visited on 02/17/2022).
- [15] Eduardo Redondo-Iglesias, Pascal Venet, and Serge Pelissier. “Eyring acceleration model for predicting calendar ageing of lithium-ion batteries”. en. In: *Journal of Energy Storage* 13 (2017), pp. 176–183. ISSN: 2352-152X. DOI: 10.1016/j.est.2017.06.009. URL: <https://www.sciencedirect.com/science/article/pii/S2352152X17300634> (visited on 02/17/2022).
- [16] Xiao-Guang Yang et al. “Modeling of lithium plating induced aging of lithium-ion batteries: Transition from linear to nonlinear aging”. en. In: *Journal of Power Sources* 360 (Aug. 2017), pp. 28–40. ISSN: 0378-7753. DOI: 10.1016/j.jpowsour.2017.05.110. URL: <https://www.sciencedirect.com/science/article/pii/S0378775317307619> (visited on 01/20/2022).
- [17] Scott G. Marquis. “Long-Term Degradation of Lithium-ion Batteries”. English. PhD thesis. Oxford: University of Oxford, 2020. (Visited on 03/04/2022).
- [18] Frank M. Kindermann et al. “A SEI Modeling Approach Distinguishing between Capacity and Power Fade”. en. In: *Journal of The Electrochemical Society* 164.12 (Aug. 2017). Publisher: IOP Publishing, E287. ISSN: 1945-7111. DOI: 10.1149/2.0321712jes. URL: <http://iopscience.iop.org/article/10.1149/2.0321712jes/meta> (visited on 01/20/2022).
- [19] Fabian Single, Arnulf Latz, and Birger Horstmann. “Identifying the Mechanism of Continued Growth of the Solid-Electrolyte Interphase”. en. In: *ChemSusChem* 11.12 (2018). \_eprint: <https://onlinelibrary.wiley.com/doi/pdf/10.1002/cssc.201800077>, pp. 1950–1955. ISSN: 1864-564X. DOI: 10.1002/cssc.201800077. URL: <https://onlinelibrary.wiley.com/doi/abs/10.1002/cssc.201800077> (visited on 02/04/2022).
- [20] Jorn M. Reniers, Grietus Mulder, and David A. Howey. “Review and Performance Comparison of Mechanical-Chemical Degradation Models for Lithium-Ion Batteries”. en. In: *Journal of The Electrochemical Society* 166.14 (Sept. 2019). Publisher: IOP Publishing, A3189. ISSN: 1945-7111. DOI: 10.1149/2.0281914jes. URL: <https://iopscience.iop.org/article/10.1149/2.0281914jes/meta> (visited on 01/19/2022).
- [21] Simon Hein, Timo Danner, and Arnulf Latz. “An Electrochemical Model of Lithium Plating and Stripping in Lithium Ion Batteries”. In: *ACS Applied Energy Materials* 3.9 (Sept. 2020). Publisher: American Chemical Society, pp. 8519–8531. DOI: 10.1021/acsaem.0c01155. URL: <https://doi.org/10.1021/acsaem.0c01155> (visited on 01/25/2022).
- [22] Ratnakumar V. Bugga and Marshall C. Smart. “Lithium Plating Behavior in Lithium-Ion Cells”. en. In: *ECS Transactions* 25.36 (Apr. 2010). Publisher: IOP Publishing, p. 241. ISSN: 1938-5862. DOI: 10.1149/1.3393860. URL: <http://iopscience.iop.org/article/10.1149/1.3393860/meta> (visited on 01/25/2022).
- [23] Simon F. Schuster et al. “Nonlinear aging characteristics of lithium-ion cells under different operational conditions”. en. In: *Journal of Energy Storage* 1 (June 2015), pp. 44–53. ISSN: 2352-152X. DOI: 10.1016/j.est.2015.05.003. URL: <https://www.sciencedirect.com/science/article/pii/S2352152X15000092> (visited on 01/25/2022).
- [24] Qianqian Liu et al. “Understanding undesirable anode lithium plating issues in lithium-ion batteries”. en. In: *RSC Advances* 6.91 (Sept. 2016). Publisher: The Royal Society of Chemistry, pp. 88683–88700. ISSN: 2046-2069. DOI: 10.1039/C6RA19482F. URL: <https://pubs.rsc.org/en/content/articlelanding/2016/ra/c6ra19482f> (visited on 01/25/2022).

- [25] Christian von Lüders et al. “Modeling of lithium plating and lithium stripping in lithium-ion batteries”. en. In: *Journal of Power Sources* 414 (Feb. 2019), pp. 41–47. ISSN: 0378-7753. DOI: 10.1016/j.jpowsour.2018.12.084. URL: <https://www.sciencedirect.com/science/article/pii/S0378775318314484> (visited on 01/27/2022).
- [26] Xianke Lin et al. “Lithium Plating Mechanism, Detection, and Mitigation in Lithium-Ion Batteries”. en. In: *Progress in Energy and Combustion Science* 87 (Nov. 2021), p. 100953. ISSN: 0360-1285. DOI: 10.1016/j.pecs.2021.100953. URL: <https://www.sciencedirect.com/science/article/pii/S0360128521000514> (visited on 04/28/2022).
- [27] Simon E. J. O’Kane et al. “Lithium-ion battery degradation: how to model it”. en. In: *Physical Chemistry Chemical Physics* 24.13 (Mar. 2022). Publisher: The Royal Society of Chemistry, pp. 7909–7922. ISSN: 1463-9084. DOI: 10.1039/D2CP00417H. URL: <http://pubs.rsc.org/en/content/articlelanding/2022/cp/d2cp00417h> (visited on 04/25/2022).
- [28] Ben Rowden and Nuria Garcia-Araez. “A review of gas evolution in lithium ion batteries”. en. In: *Energy Reports*. 4th Annual CDT Conference in Energy Storage & Its Applications 6 (2020), pp. 10–18. ISSN: 2352-4847. DOI: 10.1016/j.egyr.2020.02.022. URL: <https://www.sciencedirect.com/science/article/pii/S2352484720301876> (visited on 03/07/2022).
- [29] Johannes Wandt et al. “Singlet oxygen evolution from layered transition metal oxide cathode materials and its implications for lithium-ion batteries”. en. In: *Materials Today* 21.8 (2018), pp. 825–833. ISSN: 1369-7021. DOI: 10.1016/j.mattod.2018.03.037. URL: <https://www.sciencedirect.com/science/article/pii/S1369702118300737> (visited on 03/07/2022).
- [30] Roland Jung et al. “Oxygen Release and Its Effect on the Cycling Stability of LiNixMnyCozO2 (NMC) Cathode Materials for Li-Ion Batteries”. en. In: *Journal of The Electrochemical Society* 164.7 (May 2017). Publisher: IOP Publishing, A1361. ISSN: 1945-7111. DOI: 10.1149/2.0021707jes. URL: <https://iopscience.iop.org/article/10.1149/2.0021707jes/meta> (visited on 03/07/2022).
- [31] Rutooj Deshpande et al. “Battery Cycle Life Prediction with Coupled Chemical Degradation and Fatigue Mechanics”. en. In: *Journal of The Electrochemical Society* 159.10 (Aug. 2012). Publisher: IOP Publishing, A1730. ISSN: 1945-7111. DOI: 10.1149/2.049210jes. URL: <http://iopscience.iop.org/article/10.1149/2.049210jes/meta> (visited on 01/28/2022).
- [32] Hao Ge et al. “Investigating Lithium Plating in Lithium-Ion Batteries at Low Temperatures Using Electrochemical Model with NMR Assisted Parameterization”. en. In: *Journal of The Electrochemical Society* 164.6 (Mar. 2017). Publisher: IOP Publishing, A1050. ISSN: 1945-7111. DOI: 10.1149/2.0461706jes. URL: <https://iopscience.iop.org/article/10.1149/2.0461706jes/meta> (visited on 03/08/2022).
- [33] Scott G. Marquis et al. “An Asymptotic Derivation of a Single Particle Model with Electrolyte”. eng. In: *Journal of the Electrochemical Society* 166.15 (2019). Place: PENNINGTON Publisher: The Electrochemical Society, A3693–A3706. ISSN: 0013-4651. DOI: 10.1149/2.0341915jes.
- [34] Chang-Hui Chen et al. “Development of Experimental Techniques for Parameterization of Multi-scale Lithium-ion Battery Models”. en. In: *Journal of The Electrochemical Society* 167.8 (Jan. 2020). Publisher: The Electrochemical Society, p. 080534. ISSN: 1945-7111. DOI: 10.1149/1945-7111/ab9050. URL: <https://doi.org/10.1149/1945-7111/ab9050> (visited on 01/25/2022).
- [35] Simon E. J. O’Kane et al. “Physical Origin of the Differential Voltage Minimum Associated with Lithium Plating in Li-Ion Batteries”. en. In: *Journal of The Electrochemical Society* 167.9 (May 2020). Publisher: IOP Publishing, p. 090540. ISSN: 1945-7111. DOI: 10.1149/1945-7111/ab90ac. URL: <http://iopscience.iop.org/article/10.1149/1945-7111/ab90ac/meta> (visited on 05/05/2022).

- [36] Valentin Sulzer et al. “Python Battery Mathematical Modelling (PyBaMM)”. en. In: *Journal of Open Research Software* 9.1 (June 2021). Number: 1 Publisher: Ubiquity Press, p. 14. ISSN: 2049-9647. DOI: 10.5334/jors.309. URL: <http://openresearchsoftware.metajnl.com/articles/10.5334/jors.309/> (visited on 02/17/2022).
- [37] — Oxford Mathematical Modelling Battery Group. URL: <http://people.maths.ox.ac.uk/chapman/battery/software/> (visited on 01/26/2022).
- [38] PyBaMM. sv. URL: <https://www.pybamm.org/> (visited on 01/26/2022).
- [39] Valentin Sulzer et al. *Python Battery Mathematical Modelling (PyBaMM)*. June 2021. DOI: 10.5334/jors.309. URL: <https://github.com/pybamm-team/PyBaMM> (visited on 01/27/2022).
- [40] *Base Battery Model — PyBaMM 22.1 documentation*. URL: [https://pybamm.readthedocs.io/en/latest/source/models/base\\_models/base\\_battery\\_model.html?highlight=model%20options#pybamm.BatteryModelOptions.options](https://pybamm.readthedocs.io/en/latest/source/models/base_models/base_battery_model.html?highlight=model%20options#pybamm.BatteryModelOptions.options) (visited on 02/18/2022).
- [41] Dennis W. Dees et al. “Analysis of the Galvanostatic Intermittent Titration Technique (GITT) as applied to a lithium-ion porous electrode”. en. In: *Journal of Power Sources*. Selected Papers presented at the 14th INTERNATIONAL MEETING ON LITHIUM BATTERIES (IMLB-2008) 189.1 (Apr. 2009), pp. 263–268. ISSN: 0378-7753. DOI: 10.1016/j.jpowsour.2008.09.045. URL: <https://www.sciencedirect.com/science/article/pii/S0378775308018387> (visited on 03/10/2022).
- [42] *scipy.optimize.least\_squares — SciPy v1.8.0 Manual*. URL: [https://docs.scipy.org/doc/scipy/reference/generated/scipy.optimize.least\\_squares.html#id9](https://docs.scipy.org/doc/scipy/reference/generated/scipy.optimize.least_squares.html#id9) (visited on 03/10/2022).
- [43] Coralia Cartis et al. “Improving the Flexibility and Robustness of Model-Based Derivative-Free Optimization Solvers”. In: *arXiv:1804.00154 [math]* (May 2018). arXiv: 1804.00154. URL: <http://arxiv.org/abs/1804.00154> (visited on 02/18/2022).
- [44] *Structural and practical identifiability analysis of partially observ...* Jan. 2013. URL: <http://archive.ph/JFdmu> (visited on 03/08/2022).
- [45] Peyman Mohatat et al. “Differential Expansion and Voltage Model for Li-ion Batteries at Practical Charging Rates”. en. In: *Journal of The Electrochemical Society* 167.11 (Jan. 2020). Publisher: The Electrochemical Society, p. 110561. ISSN: 1945-7111. DOI: 10.1149/1945-7111/aba5d1. URL: <https://doi.org/10.1149/1945-7111/aba5d1> (visited on 04/25/2022).
- [46] C. Capiglia et al. “<sup>7</sup>Li and <sup>19</sup>F diffusion coefficients and thermal properties of non-aqueous electrolyte solutions for rechargeable lithium batteries”. en. In: *Journal of Power Sources* 81-82 (Sept. 1999), pp. 859–862. ISSN: 0378-7753. DOI: 10.1016/S0378-7753(98)00237-7. URL: <https://www.sciencedirect.com/science/article/pii/S0378775398002377> (visited on 04/25/2022).
- [47] M. Safari et al. “Multimodal Physics-Based Aging Model for Life Prediction of Li-Ion Batteries”. en. In: *Journal of The Electrochemical Society* 156.3 (Dec. 2008). Publisher: IOP Publishing, A145. ISSN: 1945-7111. DOI: 10.1149/1.3043429. URL: <http://iopscience.iop.org/article/10.1149/1.3043429/meta> (visited on 03/01/2022).
- [48] Harry J. Ploehn, Premanand Ramadass, and Ralph E. White. “Solvent Diffusion Model for Aging of Lithium-Ion Battery Cells”. en. In: *Journal of The Electrochemical Society* 151.3 (Feb. 2004). Publisher: IOP Publishing, A456. ISSN: 1945-7111. DOI: 10.1149/1.1644601. URL: <http://iopscience.iop.org/article/10.1149/1.1644601/meta> (visited on 03/01/2022).

## A Appendix

### A.1 Figures

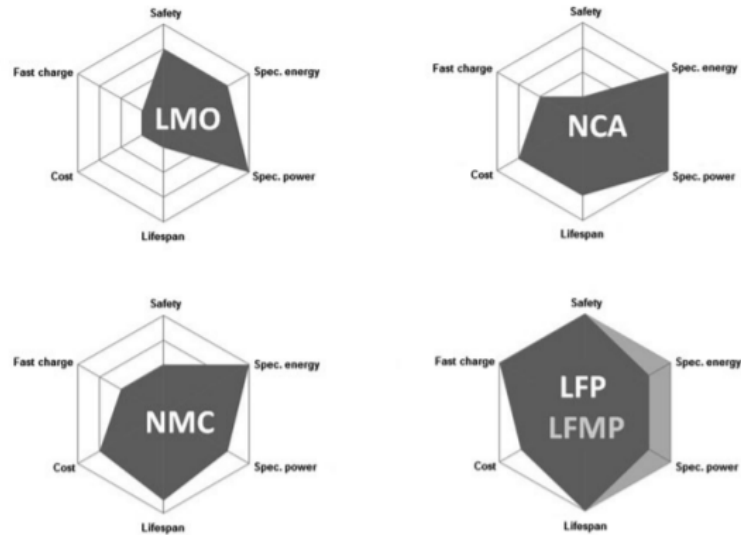


Figure 28: LIB cathode comparison between compositions listed in Table 1.[3]

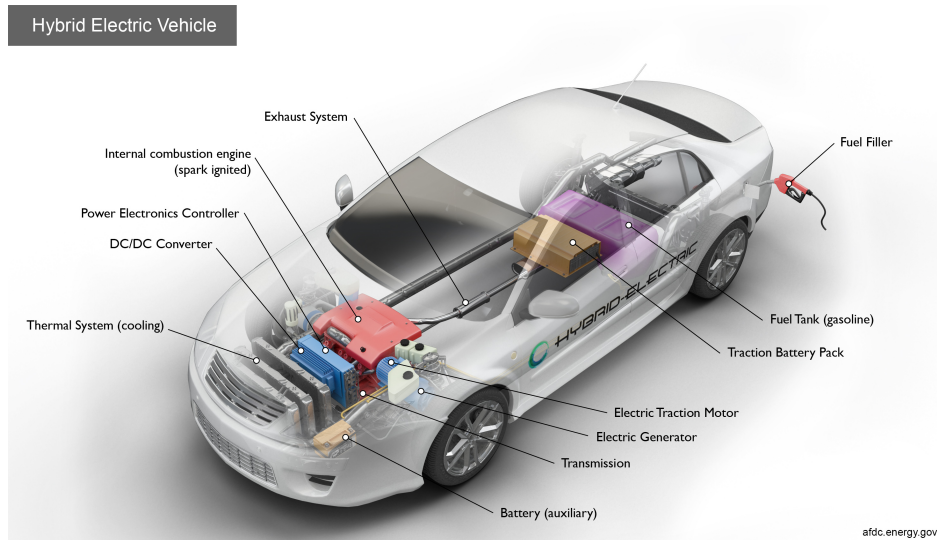


Figure 29: Components for HEV technology.[11]

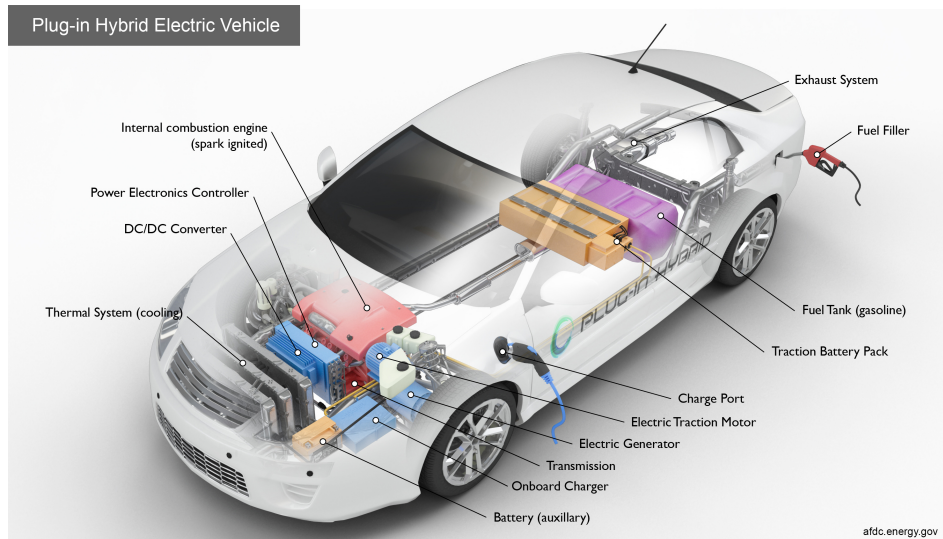


Figure 30: Components for PHEV technology.[10]

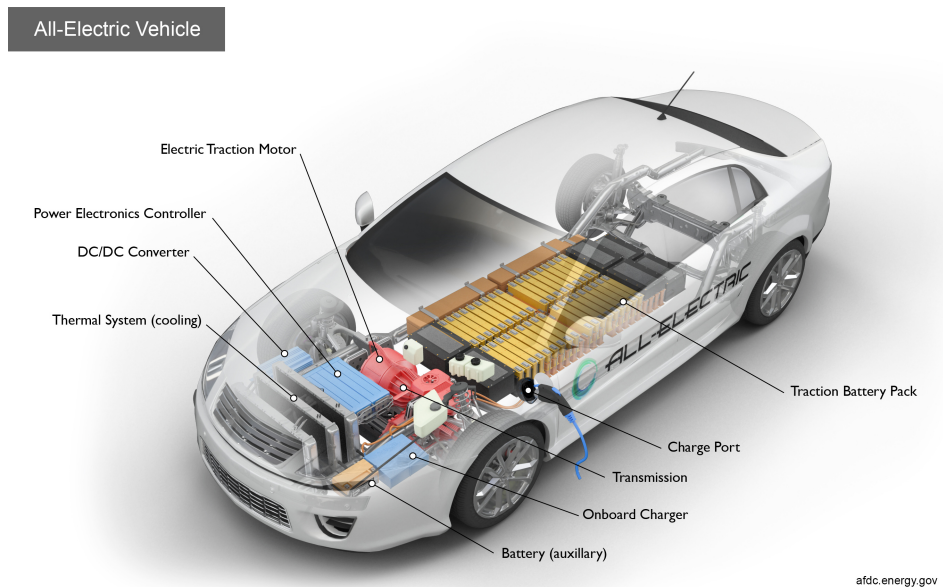


Figure 31: Components for BEV technology.[12]

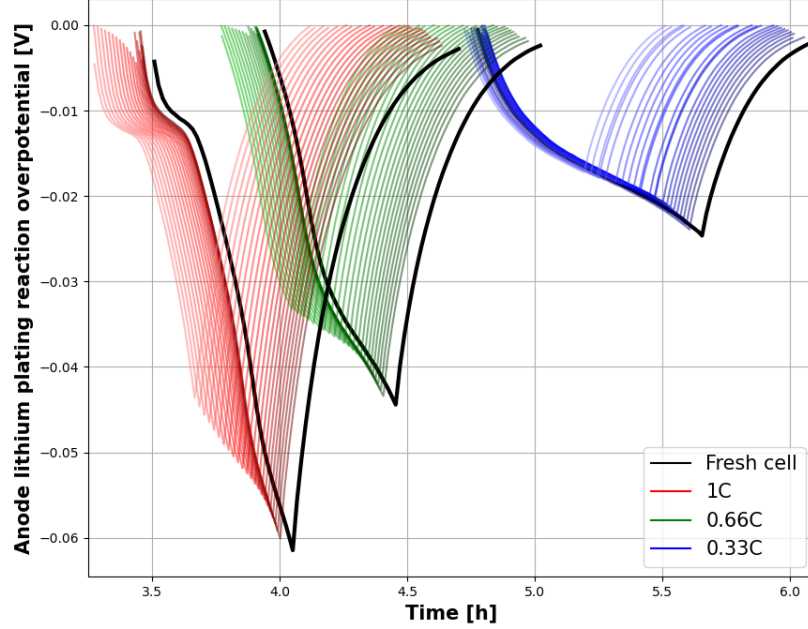


Figure 32: Visualization of lithium plating reaction overpotential reaches negative values and lithium plating formation is significantly increased. A summary of the difference between the initial cycle and the 1200th cycle can be observed in Table 11.

## A.2 Governing Equations for DFN Model

The governing equations for the DFN model will be presented below. The subscript “\*” describes a unit with dimensional quantities. The boundaries of n,s and p describes the regions within the cell negative electrode, separator, and positive electrode respectively. The additional subscript “e” describes electrolyte parameters and “s” describes solid phase parameters. A full derivation and explanations for the equations can be found in the referenced article. [33]

### Charge Conversion [33]

$$\begin{aligned} \frac{\partial i_{e,k}^*}{\partial x^*} &= \begin{cases} a_k^* j; *k & k = n, p \\ 0, & k = s \end{cases} \quad k \in \{n, s, p\} \\ i_{e,k}^* &= \epsilon_k^b \kappa_e^* (c_{e,k}^*) \left( -\frac{\partial \phi_{e,k}^*}{\partial x} + 2(1-t^+) \frac{R^* T^*}{F^*} \frac{\partial}{\partial x^*} (\log(c_{e,k}^*)) \right) \quad k \in \{n, s, p\} \\ I^* - i_{e,k}^* &= -\sigma_k^* \frac{\partial \phi_{s,k}^*}{\partial x^*} \quad k \in \{n, p\} \end{aligned}$$

### Molar Conversion [33]

$$\begin{aligned}\epsilon_k \frac{\partial c_{e,k}^*}{\partial t^*} &= \frac{\partial N_{e,k}^*}{\partial x^*} + \frac{1}{F^*} \frac{\partial i_{e,k}^*}{\partial x^*} \quad k \in \{n, s, p\} \\ N_{e,k}^* &= \epsilon_k^b D_e^* (c_{e,k}^*) \frac{\partial c_{e,k}^*}{\partial x^*} + \frac{t^+}{F^*} i_{e,k}^* \quad k \in \{n, s, p\} \\ \frac{\partial c_{s,k}^*}{\partial t^*} &= \frac{1}{(r^*)^2} \frac{\partial}{\partial r^*} \left( (r^*)^2 D_{s,k}^* \frac{\partial c_{s,k}^*}{\partial r^*} \right) \quad k \in \{n, p\}\end{aligned}$$

### Electrochemical Reactions [33]

$$\begin{aligned}j_k^* &= j_{0,k}^* \sinh \left( \frac{F^* \eta_k^*}{2R^* T^*} \right) \quad k \in \{n, p\} \\ j_{0,k}^* &= m_k^* (c_{s,k}^*)^{1/2} (c_{s,k,max}^* - c_{s,k}^*)^{1/2} (c_{e,k}^*)^{1/2} \quad k \in \{n, p\} \\ \eta_k^* &= \phi_{s,k} - \phi_{e,k} - U_k^* (c_{s,k}^*|_{r^*=R_k^*}) \quad k \in \{n, p\}\end{aligned}$$

### Boundary Conditions [33]

#### Current

$$\begin{aligned}i_{e,n}^*|_{x^*=0} &= i_{e,p}^*|_{x^*=L^*} = 0 \\ \phi_{e,n}^*|_{x^*=L_n^*} &= \phi_{e,s}^*|_{x^*=L_n^*}, \quad i_{e,n}^*|_{x^*=L_N^*} = i_{e,s}^*|_{x^*=L_N^*} = I^* \\ \phi_{e,s}^*|_{x^*=L^*-L_p^*} &= \phi_{e,p}^*|_{x^*=L^*-L_p^*}, \quad i_{e,s}^*|_{x^*=L^*-L_p^*} = i_{e,p}^*|_{x^*=L^*-L_p^*} = I^*\end{aligned}$$

### Concentration Electrolyte [33]

$$\begin{aligned}N_{e,n}^*|_{x^*=0} &= 0, \quad N_{e,p}^*|_{x^*=L^*} = 0 \\ c_{e,n}^*|_{x^*=L_n^*} &= c_{e,s}^*|_{x^*=L_n^*}, \quad N_{e,n}^*|_{x^*=L_n^*} = N_{e,s}^*|_{x^*=L_n^*} \\ c_{e,s}^*|_{x^*=L^*-L_p^*} &= c_{e,p}^*|_{x^*=L^*-L_p^*}, \quad N_{e,s}^*|_{x^*=L^*-L_p^*} = N_{e,p}^*|_{x^*=L^*-L_p^*}\end{aligned}$$

### Concentration of active material in electrode [33]

$$\frac{\partial c_{s,k}^*}{\partial r^*}|_{r^*=0} = 0, \quad -D_{s,k}^* \frac{\partial c_{s,k}^*}{\partial r^*}|_{r^*=R_k^*} = \frac{j_k^*}{F^*}$$

### Reference Potential [33]

$$\phi_{s,n}^*|_{x^*=0} = 0$$

### Initial conditions [33]

$$c_{s,k}^*(x^*, r^*, 0) = c_{s,k,0}^* \quad k \in \{n, p\}$$

$$c_{e,k}^*(x^*, 0) = c_{e,typ}^* \quad k \in \{n, s, p\}$$

## A.3 PyBaMM Parameters

### A.3.1 Cell

#### Macroscale geometry

Negative current collector thickness [m]

Separator thickness [m]

Positive electrode thickness [m]

Positive current collector thickness [m]

Electrode height [m]

Electrode width [m]

Cell cooling surface area [ $m^2$ ]

Cell volume [ $m^3$ ]

#### Current collector properties

Negative current collector conductivity [ $S \cdot m^{-1}$ ]

Positive current collector conductivity [ $S \cdot m^{-1}$ ]

#### Density

Negative current collector density [ $kg \cdot m^{-3}$ ]

Positive current collector density [ $kg \cdot m^{-3}$ ]

#### Specific heat capacity

Negative current collector density [ $J \cdot kg^{-1} K^{-1}$ ]

Negative current collector density [ $J \cdot kg^{-1} K^{-1}$ ]

#### Thermal conductivity

Positive current collector thermal conductivity [ $W \cdot m^{-1} K^{-1}$ ]

Negative current collector thermal conductivity [ $W \cdot m^{-1} K^{-1}$ ]

#### Electrical

Nominal cell capacity [Ah]

Typical current [A]

Current function [A]

### A.3.2 Electrolyte

#### Electrolyte Properties

Typical electrolyte concentration [ $mol \cdot m^{-3}$ ]

Cation transference number

Electrolyte diffusivity [ $m^2 \cdot s^{-1}$ ]

Electrolyte conductivity [ $S^2 \cdot m^{-1}$ ]

### A.3.3 Experiment

#### Temperature

Reference temperature [K]

Total heat transfer coefficient [ $W \cdot m^{-2} \cdot K^{-1}$ ]

Ambient temperature [K]

#### **Electrical**

Number of electrodes connected in parallel to make a cell

Number of cells connected in series to make a battery

Lower voltage cut-off [V]

Upper voltage cut-off [V]

#### **Initial conditions**

Initial concentration in negative electrode [ $mol \cdot m^{-3}$ ]

Initial concentration in positive electrode [ $mol \cdot m^{-3}$ ]

Initial concentration in electrolyte [ $mol \cdot m^{-3}$ ]

Initial temperature [K]

### **A.3.4 Negative electrode**

#### **Electrode properties**

Negative electrode conductivity [ $S^2 \cdot m^{-1}$ ]

Maximum concentration in negative electrode [ $mol \cdot m^{-3}$ ]

Negative electrode diffusivity [ $m^2 \cdot s^{-1}$ ]

Negative electrode OCP [V]

#### **Microstructure**

Negative electrode porosity

Negative electrode active material volume fraction

Negative particle radius [m]

Negative electrode Bruggeman coefficient (electrolyte)

Negative electrode Bruggeman coefficient (electrode)

#### **Interfacial reactions**

Negative electrode cation signed stoichiometry

Negative electrode electrons in reaction

Negative electrode charge transfer coefficient

Negative electrode double-layer capacity [ $F \cdot m^{-2}$ ]

Negative electrode exchange-current density [ $A \cdot m^{-2}$ ]

#### **Negative electrode density**

Negative electrode density [ $kg \cdot m^{-3}$ ]

#### **Thermal parameters**

Negative electrode specific heat capacity [ $J \cdot kg^{-1} K^{-1}$ ]

Negative electrode thermal conductivity [ $W \cdot m^{-1} K^{-1}$ ]

Negative electrode OCP entropic change [ $V \cdot K^{-1}$ ]

### **A.3.5 Positive electrode**

#### **Electrode properties**

Positive electrode conductivity [ $S^2 \cdot m^{-1}$ ]

Maximum concentration in negative electrode [ $mol \cdot m^{-3}$ ]

Positive electrode diffusivity [ $m^2 \cdot s^{-1}$ ]

Positive electrode OCP [V]

#### **Microstructure**

Positive electrode porosity

Positive electrode active material volume fraction

Positive particle radius [m]

Positive electrode Bruggeman coefficient (electrolyte)  
Positive electrode Bruggeman coefficient (electrode)

#### Interfacial reactions

Positive electrode cation signed stoichiometry  
Positive electrode electrons in reaction  
Positive electrode charge transfer coefficient  
Positive electrode double-layer capacity [ $F \cdot m^{-2}$ ]  
Positive electrode exchange-current density [ $A \cdot m^{-2}$ ]

#### Positive electrode density

Positive electrode density [ $kg \cdot m^{-3}$ ]

#### Thermal parameters

Positive electrode specific heat capacity [ $J \cdot kg^{-1} K^{-1}$ ]  
Positive electrode thermal conductivity [ $W \cdot m^{-1} K^{-1}$ ]  
Positive electrode OCP entropic change [ $V \cdot K^{-1}$ ]

### A.3.6 Separator

Separator porosity  
Separator Bruggeman coefficient (electrolyte)  
Separator density [ $kg \cdot m^{-3}$ ]  
Separator specific heat capacity [ $J \cdot kg^{-1} K^{-1}$ ]  
Separator thermal conductivity [ $W \cdot m^{-1} K^{-1}$ ]

### A.3.7 Lithium plating

Lithium metal partial molar volume [ $m^3 \cdot mol^{-1}$ ]  
Lithium plating kinetic rate constant [ $m \cdot s^{-1}$ ]  
Exchange-current density for plating [ $A \cdot m^{-2}$ ]  
Exchange-current density for stripping [ $A \cdot m^{-2}$ ]  
Initial plated lithium concentration [ $mol \cdot m^{-3}$ ]  
Typical plated lithium concentration [ $mol \cdot m^{-3}$ ]

### A.3.8 SEI

#### SEI properties

Inner SEI reaction proportion  
Inner SEI partial molar volume [ $m^3 \cdot mol^{-1}$ ]  
Outer SEI partial molar volume [ $m^3 \cdot mol^{-1}$ ]  
SEI reaction exchange current density [ $A \cdot m^{-2}$ ]  
SEI resistivity [ $\Omega \cdot m$ ]  
Outer SEI solvent diffusivity [ $m^2 \cdot s^{-1}$ ]  
Bulk solvent concentration [ $mol \cdot m^{-3}$ ]  
Ratio of inner and outer SEI exchange current densities  
Inner SEI open-circuit potential [V]  
Outer SEI open-circuit potential [V]  
Inner SEI electron conductivity [ $S \cdot m^{-1}$ ]  
Inner SEI lithium interstitial diffusivity [ $m^2 \cdot s^{-1}$ ]  
Lithium interstitial reference concentration [ $mol \cdot m^{-3}$ ]  
Initial inner SEI thickness [m]

|  |
|--|
| Initial outer SEI thickness [ $m$ ]                                    |
| EC initial concentration in electrolyte [ $mol \cdot m^{-3}$ ]         |
| EC diffusivity [ $m^2 \cdot s^{-1}$ ]                                  |
| SEI kinetic rate constant [ $m \cdot s^{-1}$ ]                         |
| SEI open-circuit potential [V]   |
| <b>Reaction-driven LAM</b>   |
| Negative electrode reaction-driven LAM factor [ $m^3 \cdot mol^{-1}$ ] |
| Positive electrode reaction-driven LAM factor [ $m^3 \cdot mol^{-1}$ ] |

### A.3.9 Standard Values of SEI Parameters

Standard parameter values that were initially fit against experimental data in the study can be viewed in 12.

Table 12: Standard SEI parameter values which is pre-installed in PyBaMM and their origin.

| SEI Parameter   | Unit                 | Value   | Origin |
|---|----------------------|---------|--------|
| Inner SEI reaction proportion                           | -                    | 0.5     | [47]   |
| Inner SEI partial molar volume                          | $m^3 \cdot mol^{-1}$ | 9.6E-5  | [47]   |
| Outer SEI partial molar volume                          | $m^3 \cdot mol^{-1}$ | 9.6E-5  | Guess  |
| SEI reaction exchange current density                   | $A \cdot m^{-2}$     | 1.5E-7  | [47]   |
| SEI resistivity   | $\Omega \cdot m$     | 2E5     | [47]   |
| Outer SEI solvent diffusivity                           | $m^2 \cdot s^{-1}$   | 2.5E-22 | [19]   |
| Bulk solvent concentration                              | $mol \cdot m^{-3}$   | 2.6E3   | [48]   |
| Ratio of inner and outer SEI exchange current densities | -                    | 1       | Guess  |
| Inner SEI open-circuit potential                        | V                    | 0.1     | Guess  |
| Outer SEI open-circuit potential                        | V                    | 0.4     | Guess  |
| Inner SEI electron conductivity                         | $S \cdot m^{-1}$     | 8.9E-14 | [19]   |
| Inner SEI lithium interstitial diffusivity              | $m^2 \cdot s^{-1}$   | 1E-20   | Guess  |
| Lithium interstitial reference concentration            | $mol \cdot m^{-3}$   | 15      | [19]   |
| Initial inner SEI thickness                             | $m$                  | 2.5E-9  | [47]   |
| Initial outer SEI thickness                             | $m$                  | 2.5E-9  | [47]   |
| EC initial concentration in electrolyte                 | $mol \cdot m^{-3}$   | 4.541E3 | [47]   |
| EC diffusivity  | $m^2 \cdot s^{-1}$   | 2E-18   | [16]   |
| SEI kinetic rate constant                               | $m \cdot s^{-1}$     | 1E-12   | [16]   |
| SEI open-circuit potential                              | V                    | 0.4     | [47]   |